THE ASTROPHYSICAL JOURNAL, 459:686–700, 1996 March 10

ENERGY DEPOSITION AND PHOTOELECTRIC EMISSION FROM THE INTERACTION OF 10 eV TO 1 MeV PHOTONS WITH INTERSTELLAR DUST PARTICLES

ELI DWEK[1] AND RANDALL K. SMITH[2,3]
Received 1993 September 24; accepted 1995 September 15

ABSTRACT

This paper presents detailed calculations of the energy deposited by energetic photons in spherical, uncharged, interstellar dust particles. The interaction of the photons in the solid creates fast electrons from photoionizations, Auger transitions, or Compton scattering, which deposit a fraction of their energy in the dust. Fluorescent transitions following a K-shell photoionization in iron also contribute to the heating. The efficiency of the dust heating depends on the initial photon energy and on the grain size and composition. Calculations are performed for carbon and silicate particles of radius 50 Å to 1 μm, irradiated by photons with energies between 10 eV, which is about equal to the threshold for the ejection of photoelectrons, and 1 MeV, beyond which pair production dominates the photon interaction in the solid. Our studies present a consistent treatment of the partitioning of the energy of photons that interact in the dust into an absorbed fraction and a fraction that is carried away by ejected electrons. The results are presented in tables listing the energy deposited in a dust particle, E_{dep}, as a function of incident photon energy, E_γ, and plots depicting the energy carried away by the ejected electrons as a function of E_γ.

The results of this work are useful for calculating dust temperature fluctuations and equilibrium dust temperatures in astrophysical environments in which the dust is exposed to hard ultraviolet and X-ray emission and for calculating the photoelectric heating of clouds exposed to similarly hard radiation fields.

Subject headings: dust, extinction — radiation mechanisms: nonthermal — ultraviolet: ISM

1. INTRODUCTION

The absorption of UV/X-rays by interstellar dust particles is a subject of considerable astrophysical interest, since it provides an important channel for the conversion of high-energy photons into infrared (IR) radiation. Analysis of this emission can then provide important information on the energy balance and dust IR emission in astrophysical environments as diverse as active galactic nuclei (Voit 1991), nebulae that are irradiated by the nonthermal emission from an embedded pulsar such as the Crab Nebula (Dwek & Werner 1981) or G320.4−1.2 (Arendt 1991), circumstellar shells around exploding stars (Dwek 1985), and supernova remnants (Shull 1980; Wheeler, Mazurek, & Sivaramakrishnan 1980; Draine & Woods 1991).

Simple estimates of dust heating by ultraviolet (UV) and soft X-rays were presented by Shull (1980) and by Wheeler et al. (1980), who calculated the IR signature of ambient dust heated by the radiative output of a supernova remnant that exploded in a molecular cloud. Similar estimates were used by Dwek and Werner (1981), who calculated the IR signature of dust swept up by the remnant and heated by the cavity radiation field. More detailed calculations on the energy deposition by X-rays were presented recently by Voit (1991), who considered the heating of dust in active galaxies.

More recently, Laor & Draine (1993) calculated the absorption and scattering efficiencies of silicate and graphite dust over the 1 Å to 1000 μm wavelength region ($E_\gamma \approx 10^{-3}$ eV to ~ 10 keV) using Mie theory, the Rayleigh-Gans approximation, or geometrical optics in the appropriate wavelength–grain size regimes. They used these results to calculate the heating rate of dust particles assuming unit efficiency for the energy deposition at these wavelengths. This assumption has only limited validity, depending on the combination of grain size and incident photon energy, since a fraction of the energy of the absorbed photon is carried away by escaping photo- or Auger electrons.

In this paper we present detailed calculations of the energy deposited by photons in the 10 eV to 1 MeV range in spherical and uncharged astronomical graphite and silicate dust. The calculation of the energy deposition by UV/X-ray photons in the dust consists of (1) determining the probability that the photon will interact with the solid and (2) calculating the fraction of the photon energy that is deposited in the solid. The method in which we calculate the photon interaction probability in the solid depends on the size of the dust particle and the energy of the incident photon. A wavelength approach using Mie scattering theory is used when the wavelength of the incident radiation is comparable to the grain radius, and an atomistic approach is used at higher energies at which molecular or solid state effects do not affect the absorption process. The interaction of the photon with the solid results in the ejection of a photoelectron and the possible creation of a cascade of Auger electrons. The energy deposited by the photoelectron as well as the Auger electrons in the solid is then calculated using formulae for the electron energy losses in solids.

The current study improves on previous ones in several important ways: (1) it presents a self-consistent treatment of the energy absorbed by the UV/X-ray photons in the dust and that carried away by the escaping electrons; (2) it takes into account the anisotropic distribution of the emerging photoelectrons; and (3) it presents a more detailed energy spectrum of the emitted Auger electrons compared to earlier calculations by Shull (1979). The effect of the aniso-

[1] Laboratory for Astronomy and Solar Physics, Code 685, NASA/Goddard Space Flight Center, Greenbelt, MD 20771; edwek@stars.gsfc.nasa.gov.
[2] Department of Physics, University of Wisconsin-Madison, Madison, WI 53706; rsmith@wisp5.physics.wisc.edu.
[3] National Science Foundation Graduate Student Fellow.

tropic distribution of the emitted photoelectrons breaks the symmetry of any given atom with respect to the incoming radiation, so that the problem cannot be reduced to the analytical solution presented by Voit (1991). Furthermore, it causes a slight enhancement in the amount of energy deposition over that expected from an anisotropic distribution of emerging photoelectrons. The magnitude of this effect is, however, small and will be discussed in § 2.2.2.

The photon interaction cross sections, electronic energy levels, and Auger transition probabilities used in the calculations were taken from the Lawrence Livermore Laboratory's Evaluated Photon Data Library (EPDL) and Evaluated Atomic Data Library (EADL). The energy deposition by the photoelectrons is presented in § 2, that deposited by the Auger electrons in § 3, the total energy deposited in the dust is presented in § 4, and the energy carried away by escaping electrons (the photoelectric energy yield) is calculated in § 5.

2. ENERGY DEPOSITION BY PRIMARY PHOTOELECTRONS

2.1. *General Considerations*

The various physical processes underlying the interaction of X-rays with matter are lucidly described by Agarwal (1979), which has extensive references to earlier work. Consider the interaction of a single photon of energy E_γ with a dust particle of radius a. Let b be the impact parameter of the incident photon (see Fig. 1). The probability that the X-ray will penetrate the solid to depth z without interacting and then interact within a distance z and $z + dz$ in the grain is given by (e.g., Reif 1965, § 12.1)

$$P(z, E_\gamma)dz = 2 \sinh (\lambda\, dz/2) \exp (-\lambda z)$$
$$\approx \lambda \exp (-\lambda z)dz \quad \text{when } \lambda\, dz \ll 1 , \qquad (1)$$

where λ is the linear attenuation coefficient (cm^{-1}) of the X-ray in the solid. This quantity is a function of photon energy and grain composition and can be written as

$$\lambda(E_\gamma) = \frac{\rho}{\mu} \sum_{A,\pi} f(\mathrm{A})\sigma(\mathrm{A}, \pi, E_\gamma) , \qquad (2)$$

where $\sigma(\mathrm{A}, \pi, E_\gamma)$ is the photon interaction cross section with atom A via an atomic process π (photoelectric, Compton, or pair production), ρ is the mass density of the solid, μ is its mean atomic weight, and $f(\mathrm{A})$ is the frequency a given atom A occurs in a unit of dust composition. The summation in equation (2) extends over the atomic constituents in the dust composition and over the relevant physical processes. For silicates, represented by an $(MgSiFe)O_4$ dust particle, $\rho = 3.3\ g\ cm^{-3}$; $\mu = 172 m_H$ (m_H = hydrogen mass); $f(\mathrm{Mg}) = f(\mathrm{Si}) = f(\mathrm{Fe}) = 1$, and $f(\mathrm{O}) = 4$. For graphite dust particles, $\rho = 2.2\ g\ cm^{-3}$; $\mu = 12 m_H$; and $f(\mathrm{C}) = 1$.

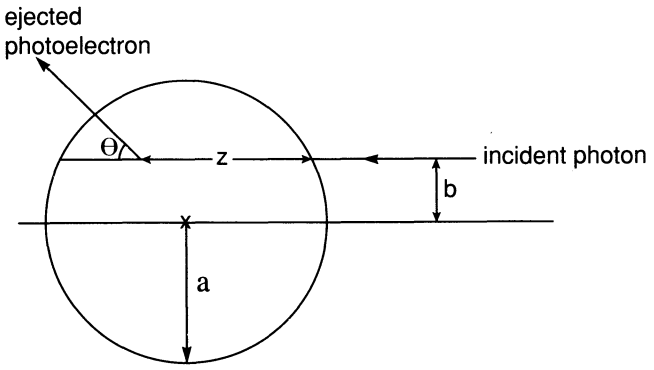

FIG. 1.—Schematic diagram depicting a photon incident on a spherical dust grain with impact parameter b. This geometrical approach is valid only when the grain size parameter $x = 2\pi a/\lambda \gg 1$. See text for details.

The total energy $E_{dep}(a, E_\gamma)$ deposited by the photon in the dust is given by the following expression:

$$E_{dep}(a, E_\gamma) = \int_V dV P(\boldsymbol{r}, E_\gamma) \times \sum_{\pi A} [\Gamma(\mathrm{A}, \pi, E_\gamma) E_d(\mathrm{A}, \pi, E_\gamma, b, z)] , \qquad (3)$$

where $E_d(\mathrm{A}, \pi, E_\gamma, b, z)$ is the energy deposited in the dust as a result of an interaction with an atom A at the location (b, z) in the dust via a particular atomic process π, $\Gamma(\mathrm{A}, \pi, E_\gamma)$ is the probability for that interaction, and the summation is over all possible atomic processes π and grain atomic constituents A. There is an implicit dependence of Γ and E_d on atomic parameters. The integral in equation (3) is over the grain volume V, and the function $P(\boldsymbol{r}, E_\gamma)$ represents the probability per unit grain volume that the incoming photon is absorbed at the location $\boldsymbol{r}$ in the dust. The method for calculating $P(\boldsymbol{r}, E_\gamma)$ depends on whether the photon behaves like a wave or like a particle in its interaction with the solid.

A particle approach to the interaction is valid when the following two conditions are met: (1) the incident photons have well-defined trajectories; and (2) the interaction of the photons with the solid can be described as a weighted sum over all interactions with the individual atoms that constitute the solid, i.e., the interaction can be expressed in terms of individual atomic cross sections. The first condition is met as long as the wavelength of the photon is small compared with the size of the particle, i.e., when $\lambda \ll a$. Defining the grain size parameter, x, as $x = 2\pi a/\lambda$, we take the transition to occur when $x = 60$, or equivalently when $E_\gamma(\mathrm{eV}) = (11.8\ \mathrm{eV})/a(\mu\mathrm{m})$. The second condition is valid as long as molecular and solid state effects, which affect the photoabsorption cross sections, can be neglected. Comparisons between experimental photoabsorption spectra for the vapor and solid phases of various elements show the absorption by solids is atomic-like at energies above 50 eV (Henke et al. 1982).

We therefore adopt for each grain of radius a a particle approach when $E_\gamma \geq E_{crit} \equiv \max\{(11.8\ \mathrm{e})/a(\mu\mathrm{m}), 50\ \mathrm{eV}\}$ and a wavelength approach at energies $E_\gamma < E_{crit}$. The probability $P(\boldsymbol{r}, E_\gamma)$ for the two energy regimes is given by

$$dV P(\boldsymbol{r}, E_\gamma) = Q_{abs}(a, E_\gamma) \frac{\boldsymbol{E}(\boldsymbol{r}) \cdot \boldsymbol{E}^*(\boldsymbol{r}) dV}{\int_V \boldsymbol{E}(\boldsymbol{r}) \cdot \boldsymbol{E}^*(\boldsymbol{r}) dV} \quad \text{when } E_\gamma \leq E_{crit} \qquad (4a)$$

$$= \frac{1}{\pi a^2} \int_0^a 2\pi b\, db \int_0^{z_0(b)} P(z, E_\gamma) dz \quad \text{when } E_\gamma \geq E_{crit} , \qquad (4b)$$

where $\int_V P(\boldsymbol{r}, E_\gamma) dV = Q_{abs}(a, E_\gamma) = E_\gamma^{-1} \int_V \boldsymbol{E}(\boldsymbol{r}) \cdot \boldsymbol{E}^*(\boldsymbol{r}) dV$ is the dust absorption efficiency which is calculated from Mie theory, $\boldsymbol{E}(\boldsymbol{r})$ is the electric field of the incoming wave at the position $\boldsymbol{r}$ in the solid and $\boldsymbol{E}^*$ is its complex conjugate. The probability $P(z, E_\gamma)$ in equation (4b) is given by equation (1), and the upper limit z_0 in the z-integral is the maximum possible penetration depth at impact parameter b, which is given by $2(r^2 - b^2)^{1/2}$ (see Fig. 1). We note that the integral of $P(\boldsymbol{r}, E_\gamma)$ over the grain volume is less than unity if the dust

particle is transparent to the incident radiation and can exceed unity when $Q_{abs} > 1$. Our approach for calculating $P(r, E_\gamma)$ in the wavelength regime ($E_\gamma \leq E_{crit}$) is identical to that used by Watson (1973) to calculate the effect of the finite grain size on the bulk photoelectric yield from solids. Details of these calculations will be presented by Smith & Dwek (1996).

We extended our calculations down to energies of 10 eV. Even in the 10 eV–E_{crit} energy interval the results incorporate some aspects of atomic theory when we calculate the relative probabilities for the various subshell transitions. However, in practice the energy deposited in the solid at these energies is dominated by the residual atomic excitation energy which does not depend on the details of the interaction. As explained in more detail below, we will assume that this residual excitation energy is absorbed in the solid. At the high end, we terminated the calculations at photon energies of 1 MeV, beyond which pair production becomes important. Within the 10 eV to 1 MeV energy range, photoelectric emission dominates the interaction of the photons with the solid at energies below ~ 50 keV, and inelastic Compton scattering dominates the interaction above that energy.

2.2. *Photoelectric Emission*

2.2.1. *Probabilities and Cross Sections*

In the energy region where photoelectric emission is the dominant means of photon interaction, the cross section for interaction with any given element A can be written as

$$\sigma_{ph}(\mathrm{A}, E_\gamma) = \sum_i P_{ph}(E_\gamma, \mathrm{A}, i)\sigma_{ph}(\mathrm{A}, i, E_\gamma) \quad (5)$$

where the sum extends over all atomic subshells i. The probability $P_{ph}(\mathrm{A}, E_\gamma)$ in this case is equal to the probability that the interaction will result in the ejection of a photoelectron from a particular subshell i of atom A and is given by

$$P_{ph}(E_\gamma, \mathrm{A}, i) = \frac{f(\mathrm{A})\sigma_{ph}(\mathrm{A}, i, E_\gamma)}{\sum_{A,i} f(\mathrm{A})\sigma_{ph}(\mathrm{A}, i, E_\gamma)} . \quad (6)$$

The kinetic energy of the ejected electron, E_k, is given by $E_\gamma - E_b(\mathrm{A}, i)$, where $E_b(\mathrm{A}, i)$ is the binding energy of electrons in the atomic subshell i of element A. Throughout this paper we will use X-ray notations to specify the electronic configuration of an atom. In standard spectroscopic notation an electronic configuration is characterized by a principal quantum number n, azimuthal quantum number $\{l\} = \{0, 1, 2 \ldots, n-1\}$, symbolically written as $\{s, p, d, \ldots\}$, and total angular momentum $j = l \pm m_s$, where $m_s = \pm \frac{1}{2}$ is the spin quantum number. The $\{n, l, j\} = \{2, 1, 3/2\}$ configuration is therefore symbolically written as $^2p_{3/2}$. In X-ray notation, the principal quantum numbers $\{n\} = \{1, 2, 3, 4, \ldots\}$ specify the shells: $\{\mathrm{K}, \mathrm{L}, \mathrm{M}, \mathrm{N}, \ldots\}$, so that the various $n = 2$ subshell: $2s_{3/2}$, $2p_{1/2}$, and $2p_{3/2}$ are in this notation written as L1, L2, and L3, respectively. Analytical fits to photoionization cross sections were presented by Verner & Yakovlev (1995); however, the photoionization cross sections for K, L, and M shells and electron binding energies used in this work were taken from Cullen et al. (1989) and D. E. Cullen (1990, private communications). The relative contribution of the various L1, L2, L3, M1, etc. subshells to the total L, M, etc. cross sections were estimated from the discontinuities in the cross sections across the appropriate threshold energies.

2.2.2. *Angular Distribution of Ejected Photoelectrons*

The ejected photoelectrons have an angular distribution which in the Born approximation is given (by Compton & Allison 1935, p. 564; and Agarwal 1979, p. 185)

$$\xi(\theta) = \frac{\sin^2(\theta)}{[1 - \beta\cos(\theta)]^4} , \quad (7)$$

where $\beta = v/c$, v is the velocity of the ejected electron, and θ is the angle between its velocity vector and the direction of the incident X-ray (see Fig. 1). The angular distribution is symmetrical in ϕ, the angle around the z-direction. The distribution function $\xi(\theta)$ peaks at an angle θ_{max} given by

$$\cos(\theta_{max}) = (2\beta)^{-1}[(1 + 8\beta^2)^{1/2} - 1] . \quad (8)$$

The maximum is at $\theta_{max} = \pi/2$ for $\beta \ll 1$ and tilts strongly in the forward direction when $\beta \to 1$. We denote by $x(\theta, \phi)$ the distance traveled by the electron before exiting the dust particle. This distance is given by

$$x(\theta, \phi) = a\left\{-\frac{b}{a} + \left[\left(\frac{b}{a}\right)^2 A^2 + B\right]^{1/2}\right\} \quad (9)$$

where

$$A = \sin\theta\cos\phi - \cos\theta\frac{\sqrt{a^2 - b^2} - z}{b} ,$$

and (10)

$$B = \frac{2z\sqrt{a^2 - b^2} - z^2}{a^2} .$$

The energy deposited by the ejected electron is obtained by integrating its energy loss function, dE/dx, over the traveled distance:

$$E_d(\theta, \phi) = \int_0^{x(\theta,\phi)} \left(\frac{dE}{dx'}\right)dx' \quad \text{if } x(\theta, \phi) > \frac{R(E_k)}{\rho}$$

$$= E_k \quad \text{if } x(\theta, \phi) < \frac{R(E_k)}{\rho} , \quad (11)$$

where $R(E)$ is the range (in g cm^{-2}) of the electron with an initial kinetic energy E, which is given by

$$R(E) = -\rho\int_0^E \left(\frac{dE}{dx}\right)^{-1} dE . \quad (12)$$

The energy $E_d(\theta, \phi)$ needs to be averaged over all possible angles θ and ϕ. For practical purposes, the energy deposition in equation (11) was calculated by assuming that all the electrons are emitted at $\theta = \theta_{max}$. The result was then averaged over all possible ϕ angles.

To examine the importance of the anisotropic distribution of the emitted photoelectrons on the energy deposited in the solid, we ran a set of models in which their angular distribution was assumed to be isotropic. The results of these calculations, performed for a grid of grain radii ranging from 50 to 1500 Å, show that the isotropic models consistently underestimate the energy deposition. The fractional error introduced by this assumption depends on the energy of the ionizing photon and the grain size. It peaks at photon energies at which the dust optical depth is about unity, and ranges from 20% to 60% for grain radii of 50 and 1500 Å, respectively.

2.2.3. *Electronic Stopping Power*

Electron ranges in various media have been calculated in the 20 eV to 10 keV energy range by Iskef, Cunningham, & Watt (1983) and by Berger & Seltzer (1964) for energies between 10 keV and 1 GeV. An analytical fit to the experimental ranges in the 20 eV to 1 MeV region was presented by Dwek (1987; eq. [3] and Fig. 1). There is a discrepancy between the figure and the equation (pointed out by Hiroshi Itoh; private communication), with the figure depicting the correct functional dependence of the range versus electron energy. Fortunately, this error did not affect the calculations in Dwek (1987) and subsequent related papers, since they used the correct functional description for the range. For purpose of this paper we derived an improved fit to the experimental data over the 20 eV to 1 MeV energy range. The resulting fits for $R(E)$ are of the form

$$\log_{10} R(E) = a_0 + \sum_{n=1}^{4} a_n \log_{10}^n (E) , \qquad (13)$$

where $R(E)$ is in units of g cm^{-2} and E is in eV. The coefficients $\{a_0, a_1, a_2, a_3, a_4\}$ in equation (13) are $\{-8.1070, 1.0596, -0.27838, 0.11741, -0.010731\}$ for graphite or carbon dust, and $\{-8.1245, 1.1102, -0.31900, 0.12908, -0.011757\}$ for silicates.

The energy deposited by a fast electron in a slab of material is then calculated in the following way. Let E_1 be the energy of the incident electron and R_0 (in g cm^{-2}) be the thickness of the material. The range R_1 of the electron can be calculated from equation (13). If $R_1 \leq R_0$, then the electron is stopped in the slab, and the energy deposited, ΔE, is simply equal to E_1. If $R_1 > R_0$, then the electron will emerge with some energy E_2, and $\Delta E = E_1 - E_2$, where E_2 is derived from equation (13) with $R = R_1 - R_0$.

3. ENERGY DEPOSITION BY AUGER ELECTRONS

3.1. *General Considerations*

The ejection of a photoelectron from a given level i creates a hole that can be filled by an electronic transition from an upper level j. The $j \rightarrow i$ transition can occur by a usual radiative process (fluorescence) or by a radiationless (Auger) transition accompanied by the ejection of a second electron (an Auger electron) from some energetically allowed level k. We will designate this Auger transition by (i, j, k), and the probability for its occurrence by $P(i, j, k)$. If j and k belong to the same shell, the transitions are referred to as Coster-Krönig transitions (e.g., Agarwal 1979). Following the initial i-shell ionization, the atom is left with an excitation energy that is equal to the subshell binding energy, E_i. Ideally, all this excitation energy should be released by the various Auger or fluorescence transitions. However, as the number of vacancies in the atom increases, some of the Auger transitions become impossible because of the lack of j or k electrons, and the atom remains in a multi-ionized, excited state. The interaction between electronic configurations will cause these states to de-excite radiatively, and the photons are most likely to be absorbed within the grain. Therefore, we will assume throughout this paper and that this residual excitation energy is absorbed in the dust (see § 3.3 for more details). Table 1 (adopted from Lee et al. 1990) lists the binding energies, E_i, for the various electronic subshells (i = K, L1, L2, etc.), the fraction of this energy that is released in the form of Auger electrons or radiative transitions, and the residual excitation energy stored in the atom after all allowable Auger and fluorescence transitions have been exhausted. For initial K-shell vacancies, the residual excitation energy constitutes a small fraction (never more than 10%) of the binding energy. For

TABLE 1

SUBSHELL BINDING ENERGIES AND RELAXATION PROCESSES FOLLOWING A SUBSHELL VACANCY[a]

ELEMENT	SUBSHELL	E_{bind} (eV)	RELAXATION PROCESS		
			X-Ray Emission	Auger Effect	Residual Excitation
Carbon	K	291.01	1.6302 (−3)	9.003 (−1)	9.8071 (−2)
	L1	17.56	0.0	0.0	1.0
Oxygen	K	537.28	6.0090 (−3)	9.1354 (−1)	8.3000 (−2)
	L1	29.23	0.0	0.0	1.0
Magnesium.....	K	1294.50	2.6346 (−2)	9.5056 (−1)	2.3084 (−2)
	L1	89.46	1.4766 (−3)	7.6860 (−1)	2.2992 (−1)
	L2	56.55	2.2632 (−3)	7.5437 (−1)	2.4336 (−1)
	L3	56.24	2.4198 (−3)	7.5289 (−1)	2.4468 (−1)
	M1	6.89	0.0	0.0	1.0
Silicon	K	1828.50	4.4613 (−2)	9.3357 (−1)	2.1814 (−2)
	L1	151.55	1.7806 (−4)	8.0028 (−1)	1.9955 (−1)
	L2	108.67	2.4491 (−4)	8.3206 (−1)	1.6770 (−1)
	L3	107.98	2.4597 (−4)	8.3139 (−1)	1.6836 (−1)
	M1	13.63	0.0	0.0	1.0
Iron	K	7083.40	3.1501 (−1)	6.7451 (−1)	1.0475 (−2)
	L1	842.96	3.5909 (−3)	9.2020 (−1)	7.6211 (−2)
	L2	733.55	4.3939 (−3)	9.3616 (−1)	5.9442 (−2)
	L3	720.69	3.8059 (−3)	9.3602 (−1)	6.0181 (−2)
	M1	101.01	1.3411 (−5)	6.4915 (−1)	3.5082 (−1)
	M2	68.04	1.9834 (−5)	6.2950 (−1)	3.7048 (−1)
	M3	66.45	1.9488 (−5)	6.2245 (−1)	3.7753 (−1)
	M4	12.91	0.0	0.0	1.0

[a] The fractions of the binding energy E_{bind}, released in the various relaxation processes, were calculated by Cullen 1989 for the infinite recombination case (see § 3 for details).

initial L- and M-shell vacancies, the residual energy can be in excess of 20% of E_i, since relative to initial K-shell vacancies, they have fewer allowed de-excitation modes. The fraction of the initial subshell binding energy that ends up as residual excitation depends on the assumptions made in the Auger calculations, a subject we discuss in some detail below.

Table 1 shows that most of the excitation energy is carried away in the form of Auger electrons, with fluorescent transitions accounting for less than 4.46% of this energy in all atoms with $Z < 14$. They were therefore ignored for all elements except iron, in which radiative transitions following a K-shell ionization can carry as much as 31.5% of the excitation energy. A description of the energy deposition calculations following a fluorescent transition will be given in § 3.4.

Lee et al. (1990) present, in addition to the information given in Table 1, the number of Auger electrons and their average energy for all elements from $Z = 6$ to 100 as a function of their initial subshell vacancy. However, the energy deposition in a dust particle with a size comparable to the range of the emerging Auger electrons requires a more detailed description of their energy distribution. To illustrate this point, consider a hypothetical dust particle consisting of pure magnesium. Suppose now than an incident photon created a K-shell vacancy in a Mg atom located at the center of the particle. The K-shell vacancy will be filled by a radiationless transition that will result in the ejection of an average number of two 577 eV Auger electrons (see Table 4; a detailed explanation of the calculations leading to the results in this table will follow). Suppose now that the grain radius is exactly equal to the stopping length of a 577 eV electron (about 100 Å). Using these average quantities we would conclude that the total energy deposited in the grain is 1154 eV. However, the detailed energy spectrum of the Auger electrons (Table 4) reveals that 97% of their energy is carried by a $\sim$1200 eV electron, with most of the remaining energy carried off by an electron with an average energy of $\sim$35 eV. The 1200 eV electron will deposit only $\sim$330 eV in the grain, so that the total energy deposited by the Auger electrons is only $\sim$365 eV instead of the 1154 eV inferred from a simple calculation that uses an average energy for the Auger electrons.

We calculated the detailed spectrum of the emerging Auger electrons, using the EADL Auger transitions probabilities. We will first discuss our calculations of the energy distribution of the primary Auger electrons for the various elements considered in this paper. These calculations are straightforward, compared with those for the electrons that are subsequently emitted, since the energy distribution of the latter electrons depends on the detailed evolution of the cascade in the presence of more than one electronic vacancy.

3.2. *Primary Auger Transitions*

Auger transitions are labeled by a set of three subshells: the first designates the initial subshell vacancy, the second, the subshell of the electron making the downward transition, and the third, the subshell from which the Auger electron is ejected. The angular distribution of the Auger electrons is isotropic, and their kinetic energy for an (i, j, k) transition is given by $E(i, j, k) = (E_i - E_j) - E_k$. Tables 2.1–2.5 list the various primary Auger transitions with their probabilities and energies for the various elements considered in this paper. These transition probabilities are calculated for single initial vacancies and are normalized so that $\mathscr{P}_i \equiv \sum_{j,k} P(i, j, k)$ is equal to the number of primary Auger electrons emitted following an i vacancy. The sum is over all allowable j and k levels. The last entry for each subshell vacancy (separated from the others by a dotted line) lists $\mathscr{P}_i$ and $\langle E_{\rm Auger}(i)\rangle$, the average kinetic energy carried away by these electrons which is given by $\sum_{j,k} P(i, j, k) \times E(i, j, k)/\mathscr{P}_i$. When primary Auger electrons dominate the yield from a given subshell, the value of $\mathscr{P}_i\langle E_{\rm Auger}\rangle_i$ calculated from Tables 2.1–2.5, should be equal to the energy released by all Auger transitions that is given in Table 1. For example, Table 2.2 lists the various primary Auger transitions following a K-shell vacancy in oxygen. The sum $\mathscr{P}_1 = \sum P(1, j, k) = 0.99382$, and the total kinetic energy carried away by the electrons is $498\mathscr{P}_1 = 495$ eV, which is equal to the fraction of the binding energy released by all Auger transitions, listed in Table 1. This equality shows that for oxygen, all Auger transitions following an initial K-shell vacancy are primary transitions. The situ-

TABLE 2.1

PRIMARY AUGER TRANSITION PROBABILITIES AND ENERGIES FOR CARBON

Transition	Probability	Energy (eV)
K L1 L1	0.41361	255.88
K L1 L23.....	0.40729	264.45
K L2 L23.....	0.11422	273.02
K L3 L23.....	0.06320	273.03
K	0.99832	262.44

TABLE 2.2

PRIMARY AUGER TRANSITION PROBABILITIES AND ENERGIES FOR OXYGEN

Transition	Probability	Energy (eV)
K L1 L1	0.17856	478.82
K L1 L23.....	0.34648	493.89
K L2 L23.....	0.30206	508.94
K L3 L23.....	0.16672	508.98
K	0.99382	498.29

TABLE 2.3

PRIMARY AUGER TRANSITION PROBABILITIES AND ENERGIES FOR MAGNESIUM

Transition	Probability	Energy (eV)
K L1 L1	0.082386	1115.58
K L1 L23	0.255136	1148.64
K L1 M1	0.012625	1198.15
K L2 L23	0.390341	1181.55
K L2 M1	0.005999	1231.06
K L3 L3	0.214390	1182.02
K L3 M1	0.011776	1231.37
K	0.97265	1168.56
L1 L2 M1	0.33128	26.02
L1 L3 M1	0.65670	26.33
L1 M1 M1.....	0.01201	75.68
L1	0.99999	26.82
L2 M1 M1.....	0.99742	42.77
L3 M1 M1.....	0.99724	42.46

TABLE 2.4

PRIMARY AUGER TRANSITION PROBABILITIES AND ENERGIES FOR SILICON

Transition	Probability	Energy (eV)
K L1 L1	0.074937	1525.40
K L1 L23	0.236702	1568.73
K L1 M123	0.019923	1668.54
K L2 L23	0.371098	1611.85
K L2 M123	0.015433	1709.31
K L3 L3	0.203490	1612.54
K L3 M123	0.030386	1709.98
K M1 M1	0.000666	1801.24
K	0.952635	1600.51
L1 L2 M1	0.263490	29.25
L1 L2 M23	0.065484	36.35
L1 L3 M1	0.519480	29.94
L1 L3 M23	0.126246	37.04
L1 M1 M1	0.010320	124.29
L1 M1 M23	0.014967	131.39
L1	0.9999	33.57
L2 M1 M1	0.067613	81.41
L2 M1 M23	0.589857	88.49
L2 M2 M23	0.334799	95.60
L2 M3 M3	0.007461	95.63
L2	0.99973	90.44
L3 M1 M1	0.065666	80.72
L3 M1 M23	0.590846	87.83
L3 M2 M23	0.138614	94.91
L3 M3 M3	0.204590	94.94
L3	0.99972	89.80

ation is different, for example, in iron, where higher order Auger transitions play an important role. Table 2.5 lists the various primary Auger transitions following a K-shell vacancy in iron. The total kinetic energy carried away by the electrons is 5725 $\mathscr{P}_1 = 3742$ eV [where $\mathscr{P}_1 = \sum P(1, j, k) = 0.6536$; the remainder is due to radiative de-excitation to the K shell; see Table 1 and § 3.2], significantly less than the value of 4778 eV (= 0.67451 × 7083.4 eV; see Table 1) carried by all Auger transitions.

3.3. *Secondary Auger Transitions*

After a primary (i, j, k) Auger transition, the atom is doubly ionized, with holes in the j and k subshells. These holes can be filled by a radiationless transition from a j' subshell resulting in the ejection of a second Auger electron from k' with kinetic energy $(E_j - E_{j'}) - E_{k'}$ or $(E_k - E_{j'}) - E_{k'}$, depending on which hole got filled by the j' electron. After this secondary Auger transition, (j, j', k') or (k, j', k'), the atom is left with vacancies in the k (or j), and j' and k' subshells, which can result in tertiary Auger transition of the kind: (j, j'', k''), (k, j'', k''), (j, j'', k'') or (k', j'', k''), and so on. The subshell vacancies increase in number and "move" outward toward higher excitation levels, until all possibly allowed Auger transitions are exhausted, and the atom is left in a multi-ionized and often excited state.

The calculations used in this paper use a deterministic (as opposed to a Monte Carlo) method to calculate the Auger yield and electron energy distribution. To illustrate our calculational method, we plotted in Figure 2 a tree diagram (*solid line*) that follows two of the possible cascade channels, (K L1 L1) and (K L1 L2), after the creation of an initial K-shell vacancy in Mg. At each branching point in the cascade (shown as filled circles in the diagram), we consider

TABLE 2.5

PRIMARY AUGER TRANSITION PROBABILITIES AND ENERGIES FOR IRON

Transition	Probability	Energy (eV)
K L1 L1	0.044166	5397.48
K L1 L23	0.138500	5511.49
K L1 M123	0.029590	6153.06
K L1 M45	0.001049	6227.70
K L2 L23	0.220053	5628.67
K L2 M123	0.031152	6274.72
K L2 M45	0.000949	6337.11
K L3 L3	0.117770	5642.02
K L3 M123	0.060201	6289.84
K L3 M45	0.003232	6349.88
K M1 M1	0.000787	6881.38
K M1 M23	0.002045	6915.35
K M2 M3	0.002616	6948.91
K M3 M3	0.001493	6950.50
K	0.653603	5725.45
L1 L2 M23	0.143996	42.29
L1 L2 M45	0.131998	96.60
L1 L3 M1	0.154710	21.26
L1 L3 M23	0.243212	55.34
L1 L3 M45	0.284090	109.44
L1 M1 M1	0.003617	640.94
L1 M1 M23	0.019286	674.96
L1 M1 M45	0.010514	729.14
L1 M2 M5	0.001121	762.18
L1 M3 M45	0.002944	763.66
L1 M4 M5	0.003267	817.31
L1 M5 M5	0.000900	817.48
L1	0.999655	96.22
L2 M1 M1	0.005710	531.53
L2 M1 M23	0.113020	564.50
L2 M1 M45	0.010671	619.75
L2 M2 M23	0.399615	598.66
L2 M2 M45	0.199571	652.71
L2 M3 M3	0.008599	600.65
L2 M3 M45	0.087477	654.21
L2 M4 M45	0.163894	707.86
L2 M5 M5	0.006972	707.90
L2	0.995529	629.10
L3 M1 M1	0005728	518.67
L3 M1 M23	0.111199	553.23
L3 M1 M45	0.011013	606.85
L3 M2 M23	0.163701	586.20
L3 M2 M45	0.043251	639.90
L3 M3 M3	0.239960	587.79
L3 M3 M45	0.245158	641.43
L3 M4 M45	0.106750	695.04
L3 M5 M5	0.069377	695.21
L3	0.996137	617.92
M1 M2 M45	0.290840	20.19
M1 M3 M45	0.612820	21.73
M1 M4 M45	0.050134	75.35
M1 M5 M5	0.046189	75.53
M1	0.999983	26.46
M2 M45 M45	0.99997	42.83
M3 M45 M45	0.99998	41.36

all possible Auger transitions (energetically allowed and with electrons present in the levels involved in the transition). We then assign a probability for a given cascade channel. If all the cascades involve transitions that fill the same vacancy, then their relative probabilities is simply taken from Table 2 (which is based on the EADL tables). This situation occurs in Figure 2 at branching points A and

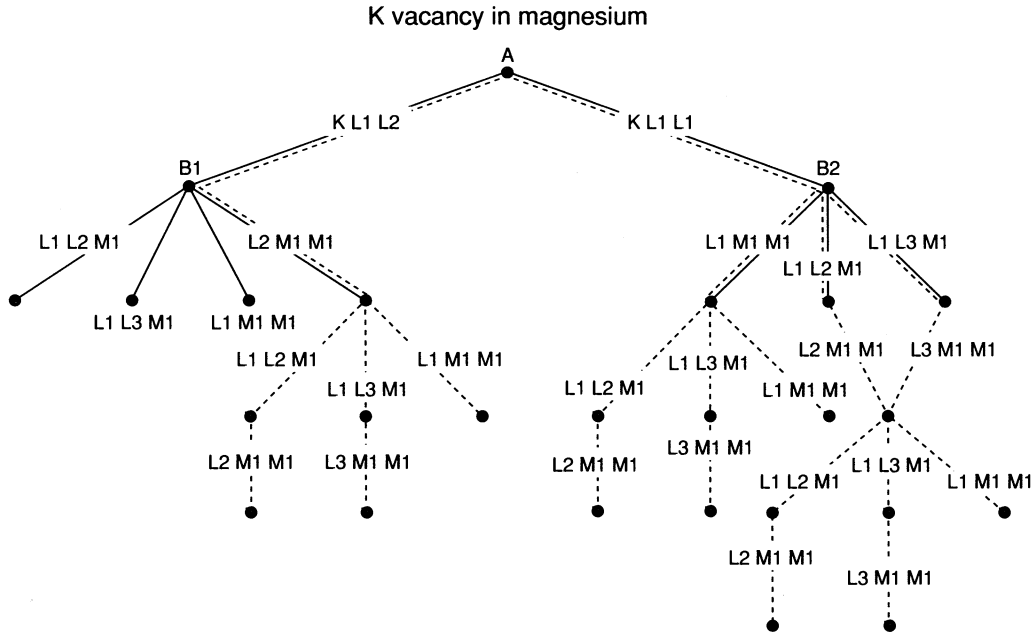

FIG. 2.—Tree diagram depicting the Auger cascade following a K-shell ionization in magnesium. The diagram is explained in detail in § 3.2 of the text.

B2 of the cascade; in the former, two transitions compete to fill the K-shell vacancy, and in the latter, three transitions compete to fill the L1 vacancy.

However, at some branching points the vacancies belong to different subshells. Such a situation occurs, for example, at branching point B1 in Figure 2, since there are competing vacancies in the L1 and L2 subshells. In these cases we calculated the various transition probabilities using the Auger transition rates presented by Opendak (1990). The ratio P(L2 M1 M1)/[P(L1 L2 M1) + P(L1 L3 M1) + P(L1 M1 M1)] was in this case taken to be 0.026/2.388 = 0.01089 (Opendak 1990, Table 2). All four transition probabilities were then renormalized to unity. Note that the two transitions filling the L1 vacancy in Opendak's table actually represent all three transitions in the denominator above (see footnote to his table).

The probabilities in Table 2 assume the presence of only a single vacancy and that all other subshells are filled. Therefore, all energetically allowed transitions can indeed take place. This is essentially the assumption made by Lee et al. (1990) in their calculations of the average energy distribution of the Auger electrons. This is clearly a simplification of the actual situations in which, after the first cascade, some subshells are only partially filled, reducing the probability for a given transition. To take the existence of these vacancies into account, we scaled down the probability for a given Auger transition if the subshell that fills the vacancy is only partially filled. In this, we followed essentially the same procedure used by Jacobs et al. (1980) and Opendak (1990). For example, the (L1 L2 M1) transition follows on the heel of the K L1 L2) transition (branch point B1 in Fig. 2). The L2 subshell is therefore already half vacant before the (L1 L2 M1) transition takes place, so we therefore reduced its probability by a factor of 2 from its tabulated value.

To check the numerical accuracy of our calculational method we examined the unrealistic case in which whenever more than one vacancy formed, Auger transitions that filled the outer vacancy were followed first. In addition, all transitions were performed assuming electrons were available in the j and k shells. In this case we needed only to resort to the probabilities listed in Table 2, since any competition between channels that filled different subshell vacancies was eliminated. This approach led to the cascade diagram shown as dashed lines in Figure 2. For example, at point B1, the Mg atom has vacancies in the L1 and L2 shells, but only the (L2 M1 M1) channel is considered in the cascade. The transition leads to two new vacancies in M1, and the cascade would have been effectively terminated if it was not for the presence of the L1 vacancy that was previously ignored. This enables the cascade to develop further via the various (L1 L23 M1 M1) transitions depicted in the diagram and the subsequent fourth-generation transitions (L23 M1 M1). The result of this model give the maximum Auger yield, since we ignored the fact that the M1 shell is actually vacant. The results of our calculations were compared to the average number of Auger electrons and their average energy presented by Lee et al. (1990), since they used a similar approach in their calculations. Our results were essentially identical to within 3% of their values.

In Table 3 we compare the average number of Auger electrons emitted following an initial subshell vacancy for various elements with the results of Lee et al. (1990) and Opendak (1990). Not surprisingly, we reproduce the results of Opendak extremely well, whereas Lee et al. (1990) overestimate the average number of electrons in some cases. For iron, we compared our results to those presented by Jacobs & Rozsnyai (1986) as well. The table shows that our results are in good agreement with their calculations.

Tables 4.1–4.2 present the detailed energy spectrum of the emerging Auger electrons. The actually calculated spectrum has a finer energy resolution than actually presented in the tables. For computational efficiency we represented closely spaced energies by a single energy of the centroid. The binning level was around 6 eV for electron energies below 100 eV and could be as large as ~150 eV for energies above ~2000 eV. The tables present average quantities of the Auger electrons: the average number of emitted electrons and their average energy. In all models, calculations were terminated when all allowable transitions took place, which in some cases left the atom in an excited state. We

TABLE 3

AVERAGE NUMBER OF AUGER ELECTRONS IN VARIOUS ELEMENTS

Element	Lee et al. (1990)	Opendak (1990)	This Work
	Initial K Shell Vacancy		
C.....	0.998	...	0.999
O	0.994	...	0.996
Mg.....	3.337	2.039	2.035
Al.....	3.290	2.273	2.282
Si	3.233	2.948	2.928
Fe.....	4.918	4.836	4.863
	4.704[a]		
	Initial L1 Shell Vacancy		
Mg.....	1.985	1.000	1.000
Al.....	1.980	1.981	1.983
Si	1.974	1.974	1.974
Fe.....	4.133	4.245	4.309
	4.480[a]		
	Initial L23 Shell Vacancy		
Mg.....	0.997	0.998	0.997
Al.....	0.999	1.000	1.000
Si	0.999	1.000	1.000
Fe.....	2.463	2.501	2.463
	2.330[a]		
	Initial M1 Vacancy		
Fe.....	1.904	1.798	1.904
	1.927[a]		
	Initial M23 Vacancy		
Fe.....	1.000	1.000	1.000
	1.000[a]		

[a] Jacobs & Rozsnyai 1986.

TABLE 4.1

ENERGY SPECTRUM OF EMITTED AUGER ELECTRONS[a]

	Following a K Shell Vacancy		Following an L1 Shell Vacancy	
Element	E(eV)	$P(E)$	E(eV)	$P(E)$
Carbon	262.4	0.9994	...	...
Oxygen	498.3	0.9959	...	...
Magnesium.....	26.23	0.4237	26.23	0.9880
	42.56	0.6340	75.68	0.0120
	75.68	0.0046	**26.82**	**1.000**
	1167.	0.9549		
	1231.	0.0178	...	...
	577.3	**2.035**	...	...
Silicon	31.25	0.3962	29.71	0.7830
	88.75	1.5690	36.78	0.1917
	128.7	0.0103	90.83	0.9744
	1595.	0.9062	128.5	0.0253
	1711.	0.0458	**61.83**	**1.974**
	1801.	0.0007	...	...
	573.	**2.928**	...	...
Iron	22.68	0.3332	22.15	0.4682
	43.14	2.2112	42.76	2.1552
	55.33	0.0626	55.33	0.2432
	89.28	0.0601	93.61	0.1623
	109.7	0.0724	109.7	0.2841
	582.9	0.9103	582.7	0.6041
	664.2	0.5597	647.1	0.2669
	5582.	0.5205	707.8	0.1252
	6258.	0.1262	**180.**	**4.309**
	6931.	0.0069	...	...
	979.8	**4.863**	...	...

[a] $P(E)$ adds up to the total number of Auger electrons emitted in the transition. Entries in bold letters present the total number of Auger electrons and their average energy.

assumed that this residual excitation energy got eventually transferred to the solid.

3.4. *Fluorescence*

Fluorescent transitions following a subshell vacancy can be neglected because of their small branching ratios except when the vacancy is in the iron K shell. In this case, the ionized iron has a 30.9% probability of filling this vacancy by X-ray emission. The larger entry of 31.5% in Table 1 reflects the additional radiative transitions associated with the cascade. We assumed that the energy of the emitted X-ray was 6.358 keV, which is the energy weighted over all possible radiative transitions, and that the photon was created in the center of the dust particle of radius a_1. We then looked up the energy deposition by 6.358 keV photons incident on a dust particle of radius a_2 chosen so that its effective range $4\rho a_2/3$ is equal to ρa_1. This energy was then added to the energy deposition of the original dust particle with the appropriate probabilities. The results showed that for all incident photon energies and grain sizes considered here, the correction to the total energy deposited in the grain was never more than 0.5% because of the small cross sections for the interactions of the 6.358 keV photon.

3.5. *Inelastic Compton Scattering*

At energies above ~ 50 keV, energy losses in the solid are dominated by inelastic Compton scattering. The dust particles are transparent in this energy region, and we assumed that the incident X-rays travel an average distance of $4a/3$ in the solid. The energy deposited in the grain due to this

TABLE 4.2

ENERGY SPECTRUM OF EMITTED AUGER ELECTRONS[a]

Element	E(eV)	$P(E)$
Following an L23 Shell Vacancy		
Magnesium.....	42.62	0.9973
Silicon	90.10	0.9997
Iron	22.54	0.1211
	42.28	1.3333
	79.21	0.0130
	591.2	0.5338
	653.3	0.2879
	707.2	0.1735
	278.8	**2.462**
Following an M1 Shell Vacancy		
Iron	22.30	0.9037
	41.94	0.9037
	79.02	0.0963
	34.49	**1.904**
Following an M23 Shell Vacancy		
Iron	42.10	1.0000

[a] $P(E)$ adds up to the total number of Auger electrons emitted in the transition. Entries in bold letters present the total number of Auger electrons and their average energy.

process is then given by

$$E_{\rm dep}(a, E_\gamma) = \frac{4a}{3}\left(\frac{dE}{dx}\right)_{\rm C}, \quad (14)$$

where $(dE/dx)_{\rm C}$ is the energy deposition in the solid due to Compton scattering. Values of this function were taken from Cullen et al. (1989).

4. RESULTS OF THE CALCULATIONS

4.1. *Energy Absorbed in the Dust*

To illustrate the characteristics of the energy deposition, we considered hypothetical dust particles made of pure carbon, oxygen, magnesium, silicon, or iron atoms. We assumed a radius of 50 Å and a uniform density of 2.2, 3.0, 1.74, 2.3, and 7.9 g cm^{-3}, respectively, for these "dust" grains. The results of the calculations are presented in Figures 3*a*–3*e*. Also shown (Fig. 3*f*) are the result of $E_{\rm dep}$ for a 50 Å silicate grain $(MgSiFe)O_4$, with a density of 3.3 g cm^{-3}. Mie calculations were used to calculate the absorption probabilities only in the silicate and carbon (assumed to be in graphitic form) grains, when the grain size parameter x was less than 60. For a radius of 50 Å this corresponds to photon energies below 2.37 keV. The particle approach was used for energies above that value. Since no optical constants exist for the hypothetical grains made of pure O, Mg, or Si, we used the particle approach at all energies, as well as for the pure ion grains.

There are four different sources of energy deposition in the grain, once a photoelectron is produced. In our graphs, these are labeled Photoelectron, Auger, Residual, and Compton. The photoelectron energy deposition depends on the energy of the incoming photon, the binding energy of the atom and shell it came from, and where it was produced in the dust (and thus how far it must travel to leave the dust). We see, then, that the energy deposited by photoelectrons (*dotted line*) drops immediately after a shell opens, since electrons coming from this shell must first overcome their binding energy. However, the hole left by the ejection will either fill via an Auger transition, releasing its potential energy to the grain (*dashed line*), or will be counted as "residual" energy (*dotted dashed line*), which is added to the total energy deposited. This choice of simply adding the residual energy to $E_{\rm dep}$ was motivated by the relative unimportance of the residual energy and the added complexity of a more accurate treatment of the fate of this energy. The final mechanism we considered is Compton scattering of the photon with a bound electron (*triple-dot-dashed* line). Note that although the final result of Compton scattering is a free electron, the process is not the same as photoejection of an electron, since the photon still exists after scattering.

By way of example, consider first the simplest case: energy deposition in pure graphite grains. Carbon has six electrons, two in the K shell, two in the L1 shell, and two in the L2 or L3 shell. Since the L2 and L3 levels have nearly equal energies for all elements (~9.0 eV for carbon), we have combined them for ease in calculation and designated them as the L23 shell. Similar approximations were made to nearly identical M subshells. The energy deposited in the dust should drop to zero at any threshold energy since the ejected electron has then zero kinetic energy (if we neglect the energy deposited by photoelectrons from previous shells). However, the carbon atom is left at an excited state, and we assumed that all this excitation energy transfers to the solid. From 10 eV to the opening of the K shell at 291.01 eV, photons can only ionize outer shell electrons; the low-energy electrons ejected nearly always stay in the grain, and no Auger electrons can be formed. Thus the energy deposition in this region is dominated by photoelectrons, which implies that the energy deposition should be proportional to the cross section for interaction multiplied by the energy of the photon (assuming no photoelectrons leave the dust). Between 10 eV and 17.56 eV (the binding energy of the L1 shell), the cross section of carbon atoms remains nearly constant, so the energy deposition rises almost linearly. After the opening of the L1 shell, the cross section drops as E_γ^{-3}. Thus the energy dependence of the energy deposition curve in this region is $(E_\gamma - E_{\rm bind})E_\gamma^{-3}$. However, once photoelectrons can escape the dust, the energy deposition decreases. This effect is evident in the gradual falloff of $E_{\rm dep}$ in the figure at an energy starting at about 200 eV, which corresponds to the energy required for an electron to transverse about half a dust radius. The energy deposition sharply increases when the photon energy gets equal to the K-shell ionization threshold. As before, the falloff in $E_{\rm dep}$ beyond the threshold reflects the combined effects of increasing grain transparency to the ejected photo- and Auger electrons, and the falloff in the photoelectric cross section with incident photon energy.

Between 291.01 eV and 30 keV, the K-shell cross section dominates. The total energy deposited by photoelectrons drops right at the shell edge, because most of the photon energy is used in removing the photoelectron which has zero kinetic energy. However, the atom is now in an excited state, and this energy is eventually returned in the form of an Auger electron or, less likely, another photon. The Auger electron itself is monoenergetic, so its energy deposition variation with the X-ray energy follows the variation of the cross section with energy (Cullen et al. 1989): $\sigma \sim E_\gamma^{-3.25}$ (at $E_{\rm Auger} = 262$ eV, the energy deposition is only slightly affected by Auger electrons escaping the dust). Once above the K-shell binding energy, the photoelectron's energy increases with that of the incident photon. The behavior of its energy deposition as a function of E_γ reflects both variations with the ionization cross section and changes in the electronic stopping power, which results in a $E_\gamma^{-4.05}$ energy dependence. Above 30 keV, Compton scattering begins to dominate the energy deposition, despite having a low (but rising) cross section. The photoelectric cross section becomes negligible beyond 30 keV.

All other figures for the pure element "dust" grains can be understood in a similar fashion as above. The silicate grain, with its large number of constituent elements and large number of subshells, exhibits the most complex behavior of $E_{\rm dep}$ versus E_γ (Fig. 3*f*). The figure exhibits a pattern which represents a combination of Figures 3*b*–3*e* with the appropriate weighing factors for the constituent elements.

The results of our calculations are given in Tables 5.1 and 5.2, which present the value of the product $Q_{\rm abs}(a, E_\gamma) \times E_{\rm dep}(E_\gamma)$ for graphite and silicate grains, respectively, for grain radii a(Å) = 50, 70, 100, 200, 500, 700, 1000, 2000, 5000, 7000, and 10^4, and a range of photon energies between 10 eV and 1 MeV. For $a = 50$ Å the tabulated values are represented in Figures 3*a* and 3*f* for, respectively, graphite and silicate grains. Probabilities for absorbing the incident photons in the dust were calculated using the wavelength approach (eq. [4*a*]) for energies below $E_{\rm crit}({\rm eV}) = 11.8/a(\mu{\rm m})$, and using the particle approach (eq. [4b]) at

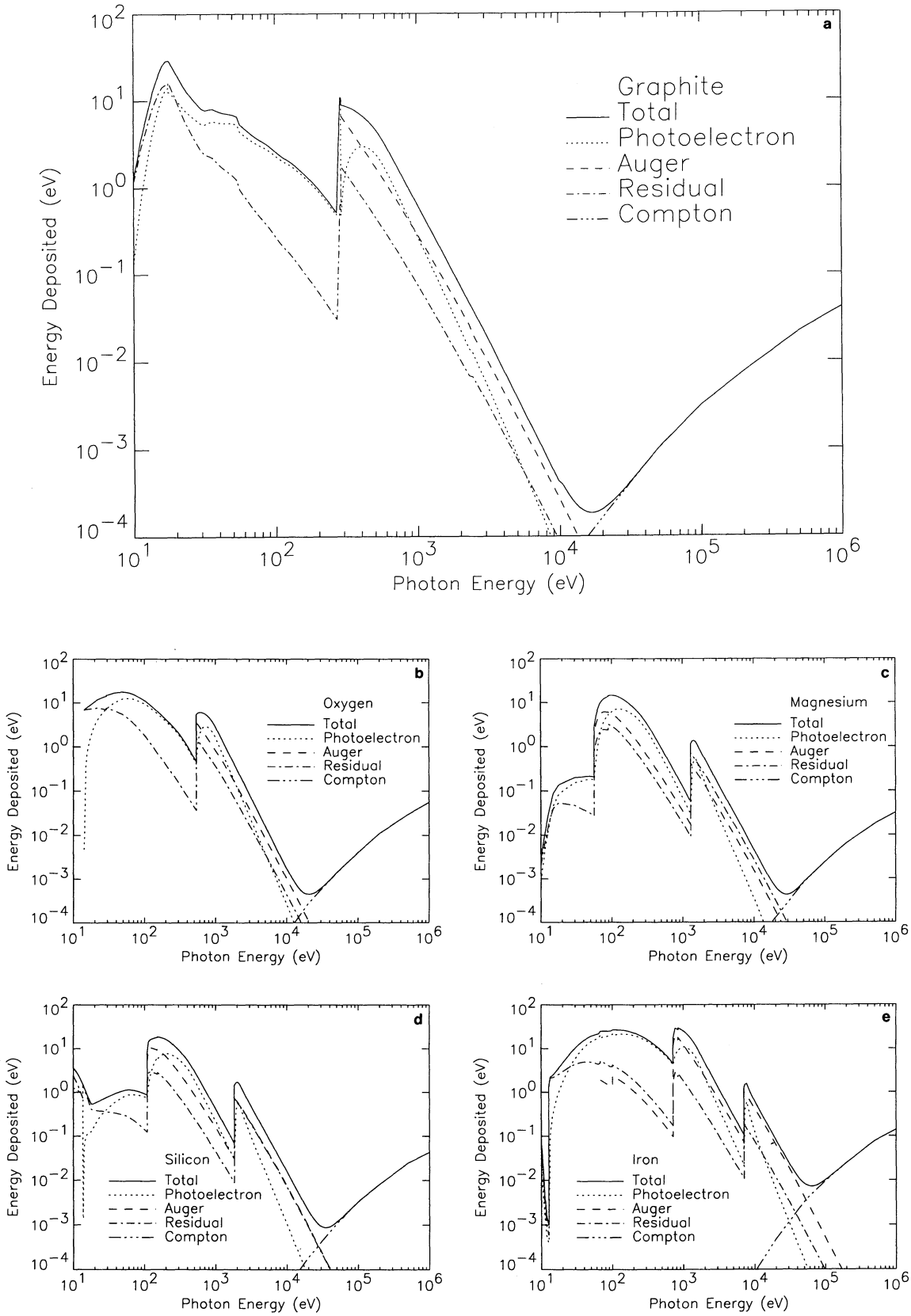

FIG. 3.—Energy deposited in a graphite grain with a radius of 50 Å is shown as a function of incident photon energy (*solid line*). For photon energies below a transitional value $E_{crit}(\text{eV}) = 11.8/a(\mu\text{m})$, determined by $x = 2\pi a/\lambda = 60$, we use Mie calculations to calculate the interaction probabilities of the photon inside the dust particle. The quantity depicted on the y-axis is then $Q_{abs}(\lambda)E_{dep}$, where $\pi a^2 Q_{abs}$ is the effective dust absorption cross section. Above the transitional photon energy, a particle approach is used to calculate the interaction probabilities of the incident photon in the dust, $Q_{abs} = 1$, and the y-axis represents the value of E_{dep}. Also shown in the figure are the contributions from the various atomic processes to the total energy deposition. (*b*) Same as (*a*) for pure oxygen spheres. For the sake of simplicity, a particle approach was used for all incident photon energies. (*c*) Same as (*b*) for pure magnesium spheres. (*d*) Same as (*b*) for pure silicon spheres. (*e*) Same as (*b*) for pure iron spheres. (*f*) Same as (*a*) for silicate grains with composition of $(MgSiFe)O_4$, except that the wavelength approach was used for energies below the transitional energy.

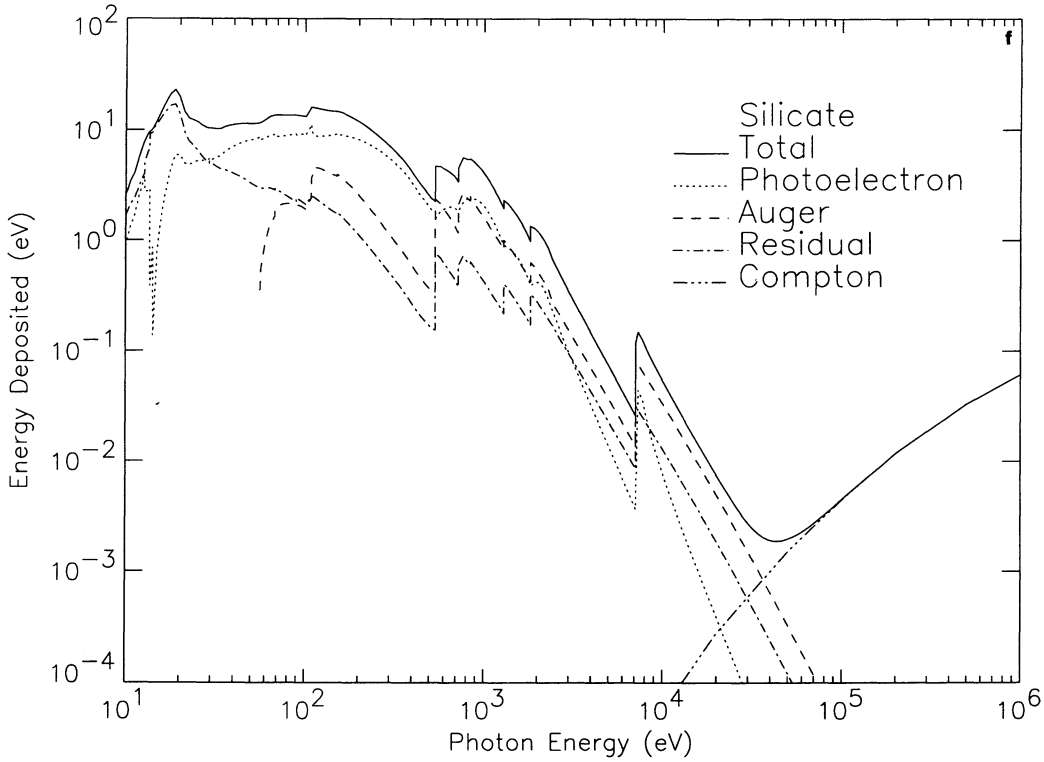

FIG. 3.—*Continued*

higher energies. Energy depositions in the wavelengths regime exhibit sometimes an oscillatory behavior with grain size, typical of Mie theory calculations in which the effective absorption cross section of the dust oscillates around its geometrical value. A consequence of this behavior is that occasionally, the energy deposited in the dust exceeds the energy of the incident photon, representing a beam-focusing effect. In the particle regime, $Q_{abs}(a, E_\gamma) = 1$.

Absorption probabilities in the wavelength regime were calculated using optical constants of graphite (Table 5.1) and silicate grains (Table 5.2). In this regime the results of Table 5.1 are strictly applicable to graphite grains. Calculations for amorphous carbon (AC) grains using the optical constants given by Rouleau & Martin (1991) show that the energy deposition in AC grains is generally smaller in the 10–20 eV region by an average factor of ~ 4 for $a = 50$ Å. In the particle regime the entries in Table 5.1 are applicable to amorphous carbon grains as well.

Figures 4 and 5 depict the fraction of the energy of the absorbed photon that is actually deposited in, respectively, graphite and silicate dust particles as a function of incident photon energy for various grain radii. Laor & Draine (1993) assumed an energy deposition efficiency of unity in their calculations (see their eq. [26]). Our results show that this assumption is valid only for large grains, where this fraction is about unity up to photon energies of ≈ 10 keV. However, as the grain radius decreases, this fraction falls below unity at progressively lower energies.

Finally, we point out that for astrophysical applications, the results of Table 5 need to be corrected for the effects of grain charge that, depending on its sign, may assist or impede the ejection of the photo- and Auger electrons from the grain's surface.

5. PHOTOELECTRIC YIELDS

A quantity of great astrophysical interest is the photoelectric energy yield, which we define here as the average energy carried away by electrons that escape the dust per incident UV/X-ray. This energy can be calculated in the following way. The probability that a photon of energy E_γ incident on a dust particle of radius a, with an impact parameter b, will emerge from the dust particle *without* interaction is given by

$$P_{esc}(a, b, E_\gamma) = 1 - \int_0^{z_0} \lambda e^{-\lambda z}\, dz\ .$$

The energy escaping the dust due to its transparency to the incident radiation, $E_{esc}(a, E_\gamma)$ is obtained by averaging the product $E_\gamma P_{esc}(a, E_\gamma)$ over all possible impact parameters b, giving

$$E_{esc}(a, E_\gamma) = \frac{E_\gamma}{\pi a^2} \int_0^a 2\pi b\, db \left(1 - \int_0^{z_0} \lambda e^{-\lambda z}\, dz\right).$$

Figure 6 shows the value of $E_{esc}(a, E_\gamma)$ as a function of incident photon energy for $a = 50$ Å and 1.0 μm graphite and silicate grains. Some effects due to the discrete nature of our calculations can be seen in the $a = 1.0$ μm cases; if the calculations could be done in a continuous fashion, we expect that the escaping energy would not fall off quite as quickly at lower energies.

We thank James Rathkopf and Rick Cullen from Lawrence Livermore Laboratory for sending us the EADL data and explaining their calculational method, Alice Trenholm for lending us her mathematical expertise, and David

1996ApJ...459..686D

TABLE 5.1

TOTAL ENERGY DEPOSITION IN GRAPHITE DUST GRAINS

E_γ (eV)	50Å	70Å	100Å	150Å	200Å	300Å	500Å	700Å	1000Å	1500Å	2000Å	3000Å	5000Å	7000Å	1.0 μm
10.00	1.3053(0)	1.9431(0)	3.1228(0)	5.8855(0)	9.7527(0)	1.4146(1)	1.5743(1)	1.4936(1)	1.3318(1)	1.1992(1)	1.1262(1)	1.0457(1)	9.7300(0)	9.3815(0)	9.0969(0)
11.00	2.8807(0)	4.4063(0)	7.3774(0)	1.3943(1)	1.8406(1)	1.8152(1)	1.6374(1)	1.4750(1)	1.3383(1)	1.2150(1)	1.1453(1)	1.0675(1)	9.9584(0)	9.6088(0)	9.3198(0)
12.00	5.4254(0)	8.2306(0)	1.3148(1)	1.9793(1)	2.0309(1)	1.9576(1)	1.6678(1)	1.5192(1)	1.3817(1)	1.2561(1)	1.1842(1)	1.1030(1)	1.0272(1)	9.8992(0)	9.5906(0)
12.73	8.0568(0)	1.2006(1)	1.7993(1)	2.2614(1)	2.1483(1)	2.0392(1)	1.7299(1)	1.5717(1)	1.4270(1)	1.2951(1)	1.2193(1)	1.1335(1)	1.0536(1)	1.0146(1)	9.8259(0)
12.75	8.1453(0)	1.2131(1)	1.8144(1)	2.2688(1)	2.1519(1)	2.0411(1)	1.7323(1)	1.5736(1)	1.4287(1)	1.2966(1)	1.2206(1)	1.1347(1)	1.0547(1)	1.0157(1)	9.8359(0)
13.62	1.2581(1)	1.8283(1)	2.4923(1)	2.5339(1)	2.3246(1)	2.1125(1)	1.8167(1)	1.6384(1)	1.4835(1)	1.3414(1)	1.2603(1)	1.1692(1)	1.0859(1)	1.0460(1)	1.0138(1)
13.64	1.2678(1)	1.8408(1)	2.5037(1)	2.5375(1)	2.3288(1)	2.1148(1)	1.8184(1)	1.6398(1)	1.4847(1)	1.3423(1)	1.2611(1)	1.1700(1)	1.0866(1)	1.0467(1)	1.0145(1)
14.00	1.4498(1)	2.0717(1)	2.7015(1)	2.5981(1)	2.4038(1)	2.1553(1)	1.8455(1)	1.6632(1)	1.5031(1)	1.3575(1)	1.2747(1)	1.1823(1)	1.0983(1)	1.0585(1)	1.0266(1)
14.18	1.5461(1)	2.1904(1)	2.7946(1)	2.6268(1)	2.4406(1)	2.1754(1)	1.8572(1)	1.6732(1)	1.5107(1)	1.3637(1)	1.2802(1)	1.1872(1)	1.1031(1)	1.0634(1)	1.0316(1)
14.20	1.5570(1)	2.2036(1)	2.8047(1)	2.6300(1)	2.4447(1)	2.1777(1)	1.8585(1)	1.6743(1)	1.5115(1)	1.3643(1)	1.2808(1)	1.1877(1)	1.1036(1)	1.0639(1)	1.0321(1)
20.00	2.0434(1)	2.3177(1)	2.3789(1)	2.3411(1)	2.2586(1)	2.0889(1)	1.8611(1)	1.7324(1)	1.6210(1)	1.5239(1)	1.4712(1)	1.4152(1)	1.3672(1)	1.3456(1)	1.3288(1)
30.00	8.1340(0)	1.0117(1)	1.2457(1)	1.5419(1)	1.7461(1)	1.9719(1)	2.1577(1)	2.2232(1)	2.2595(1)	2.2775(1)	2.2825(1)	2.2842(1)	2.2828(1)	2.2812(1)	2.2795(1)
45.00	7.1232(0)	9.3955(0)	1.2447(1)	1.6503(1)	1.9791(1)	2.4680(1)	3.0438(1)	3.3395(1)	3.5579(1)	3.7056(1)	3.7673(1)	4.4883(1)	4.4994(1)	4.5000(1)	4.5000(1)
56.23	5.3150(0)	7.2137(0)	9.7888(0)	1.3596(1)	1.6955(1)	2.2614(1)	3.0733(1)	3.5989(1)	4.0768(1)	4.4671(1)	4.6445(1)	5.5678(1)	5.6168(1)	5.6223(1)	5.6230(1)
56.25	5.3124(0)	7.2103(0)	9.7846(0)	1.3591(1)	1.6950(1)	2.2609(1)	3.0732(1)	3.5990(1)	4.0775(1)	4.4684(1)	4.6460(1)	5.5697(1)	5.6188(1)	5.6242(1)	5.6250(1)
68.03	4.0970(0)	5.6462(0)	7.7999(0)	1.1188(1)	1.4327(1)	1.9937(1)	2.8973(1)	3.5770(1)	4.3010(1)	5.0240(1)	6.3549(1)	6.6397(1)	6.7743(1)	6.7973(1)	6.8025(1)
68.05	4.0955(0)	5.6441(0)	7.7973(0)	1.1184(1)	1.4324(1)	1.9933(1)	2.8970(1)	3.5768(1)	4.3011(1)	5.0247(1)	6.3564(1)	6.6414(1)	6.7763(1)	6.7993(1)	6.8045(1)
90.00	3.0304(0)	4.2441(0)	6.0217(0)	8.8694(0)	1.1596(1)	1.6722(1)	2.5762(1)	3.3450(1)	4.2884(1)	6.6709(1)	7.4323(1)	8.2359(1)	8.7745(1)	8.9217(1)	8.9819(1)
101.00	2.5872(0)	3.6623(0)	5.2380(0)	7.7828(0)	1.0236(1)	1.4923(1)	2.3427(1)	3.0924(1)	4.0563(1)	6.6388(1)	7.5956(1)	8.7249(1)	9.6134(1)	9.9007(1)	1.0040(2)
101.02	2.5864(0)	3.6613(0)	5.2366(0)	7.7809(0)	1.0233(1)	1.4920(1)	2.3422(1)	3.0919(1)	4.0558(1)	6.6387(1)	7.5958(1)	8.7256(1)	9.6148(1)	9.9024(1)	1.0042(2)
108.66	2.3482(0)	3.3509(0)	4.8126(0)	7.1840(0)	9.4797(0)	1.3896(1)	2.2028(1)	2.9326(1)	3.8926(1)	6.5425(1)	7.6078(1)	8.9487(1)	1.0113(2)	1.0530(2)	1.0751(2)
108.68	2.3477(0)	3.3502(0)	4.8116(0)	7.1826(0)	9.4779(0)	1.3893(1)	2.2024(1)	2.9322(1)	3.8922(1)	6.5422(1)	7.6078(1)	8.9492(1)	1.0114(2)	1.0531(2)	1.0753(2)
120.00	2.1075(0)	3.0422(0)	4.3952(0)	6.5982(0)	8.7415(0)	1.2883(1)	2.0633(1)	2.7707(1)	4.7722(1)	6.3294(1)	7.5133(1)	9.1245(1)	1.0710(2)	1.1362(2)	1.1747(2)
140.00	1.7559(0)	2.5817(0)	3.7732(0)	5.7114(0)	7.6084(0)	1.1294(1)	1.8326(1)	2.4892(1)	4.2711(1)	5.8534(1)	7.1446(1)	9.0867(1)	1.1354(2)	1.2489(2)	1.3286(2)
200.00	9.8310(-1)	1.5270(0)	2.3280(0)	3.6123(0)	4.8715(0)	7.3503(0)	1.2175(1)	2.2097(1)	3.0859(1)	4.4404(1)	5.6771(1)	7.8214(1)	1.1105(2)	1.3415(2)	1.5701(2)
250.00	6.1441(-1)	1.0252(0)	1.6174(0)	2.5900(0)	3.5255(0)	5.3705(0)	1.1988(1)	1.6777(1)	2.3782(1)	3.4858(1)	4.5359(1)	6.4661(1)	9.7298(1)	1.2359(2)	1.5394(2)
291.00	1.0509(1)	1.8243(1)	2.9549(1)	4.6662(1)	6.2183(1)	8.9345(1)	9.7346(0)	1.3680(1)	1.9535(1)	2.8938(1)	3.7938(1)	5.4992(1)	8.5219(1)	1.1114(2)	1.4340(2)
291.02	8.9185(0)	1.5422(1)	2.5730(1)	4.1831(1)	5.7113(1)	8.5689(1)	1.3528(2)	1.7049(2)	2.0824(2)	2.4388(2)	2.6282(2)	2.8070(2)	2.8896(2)	2.9053(2)	2.9096(2)
350.00	7.9835(0)	1.3188(1)	2.1435(1)	3.4597(1)	4.7376(1)	7.1958(1)	1.2044(2)	1.5732(2)	2.0126(2)	2.5074(2)	2.8219(2)	3.1698(2)	3.3998(2)	3.4640(2)	3.4912(2)
500.00	4.8256(0)	8.1173(0)	1.3243(1)	2.1612(1)	2.9841(1)	5.0451(1)	8.4842(1)	1.1622(2)	1.5862(2)	2.1743(2)	2.6520(2)	3.3587(2)	4.1468(2)	4.5262(2)	4.7833(2)
537.27	4.1310(0)	7.1390(0)	1.1797(1)	1.9474(1)	2.6998(1)	4.5970(1)	7.7939(1)	1.0740(2)	1.4804(2)	2.0586(2)	2.5426(2)	3.2925(2)	4.1955(2)	4.6731(2)	5.0255(2)
537.29	4.1306(0)	7.1385(0)	1.1797(1)	1.9473(1)	2.6996(1)	4.5967(1)	7.7935(1)	1.0740(2)	1.4804(2)	2.0585(2)	2.5425(2)	3.2924(2)	4.1955(2)	4.6732(2)	5.0256(2)
650.00	2.4234(0)	4.5117(0)	8.0097(0)	1.3820(1)	2.1379(1)	3.4410(1)	5.9683(1)	8.3645(1)	1.1759(2)	1.6914(2)	2.1501(2)	2.9283(2)	4.0519(2)	4.7857(2)	5.4590(2)
720.68	1.7871(0)	3.3763(0)	6.2695(0)	1.1328(1)	1.7412(1)	2.8491(1)	5.0153(1)	7.0961(1)	1.0077(2)	1.4696(2)	1.8939(2)	2.6391(2)	3.8003(2)	4.6342(2)	5.4816(2)
720.70	1.7870(0)	3.3760(0)	6.2691(0)	1.1327(1)	1.7412(1)	2.8492(1)	5.0154(1)	7.0963(1)	1.0077(2)	1.4697(2)	1.8939(2)	2.6392(2)	3.8004(2)	4.6344(2)	5.4818(2)
850.00	1.0679(0)	2.0040(0)	3.8421(0)	8.0886(0)	1.2219(1)	2.0597(1)	3.7389(1)	5.3660(1)	7.7487(1)	1.1501(2)	1.5059(2)	2.1638(2)	3.2724(2)	4.1699(2)	5.2032(2)
1100.00	4.8001(-1)	8.8979(-1)	1.6756(0)	3.7912(0)	6.2014(0)	1.1423(1)	2.2088(1)	3.2726(1)	4.8524(1)	7.4120(1)	9.8931(1)	1.4640(2)	2.3431(2)	3.1270(2)	4.1610(2)
1294.40	2.8776(-1)	5.3052(-1)	1.0498(0)	2.1569(0)	3.6454(0)	7.2413(0)	1.5027(1)	2.2824(1)	3.4556(1)	5.3794(1)	7.2686(1)	1.0934(2)	1.7892(2)	2.4408(2)	3.3338(2)
1294.60	2.8762(-1)	5.3026(-1)	1.0492(0)	2.1557(0)	3.6434(0)	7.2380(0)	1.5021(1)	2.2816(1)	3.4545(1)	5.3777(1)	7.2664(1)	1.0931(2)	1.7887(2)	2.4402(2)	3.3330(2)
1350.00	2.5219(-1)	4.6436(-1)	9.1338(-1)	1.8672(0)	3.1478(0)	6.3807(0)	1.3511(1)	2.0686(1)	3.1546(1)	4.9405(1)	6.6952(1)	1.0114(2)	1.6624(2)	2.2782(2)	3.1298(2)
1500.00	1.8152(-1)	3.3325(-1)	6.4573(-1)	1.3060(0)	2.1701(0)	4.5497(0)	1.0223(1)	1.6113(1)	2.4986(1)	3.9778(1)	5.4237(1)	8.2838(1)	1.3757(2)	1.9036(2)	2.6506(2)
1828.40	9.7245(-2)	1.8122(-1)	3.3856(-1)	6.7410(-1)	1.1000(0)	2.2588(0)	5.7055(0)	9.6111(0)	1.5677(1)	2.5805(1)	3.5957(1)	5.5929(1)	9.5128(1)	1.3302(2)	1.8865(2)
1828.60	9.7211(-2)	1.8116(-1)	3.3844(-1)	6.7386(-1)	1.0996(0)	2.2580(0)	5.7035(0)	9.6082(0)	1.5673(1)	2.5799(1)	3.5949(1)	5.5917(1)	9.5108(1)	1.3299(2)	1.8861(2)
2000.00	7.3152(-2)	1.3600(-1)	2.5322(-1)	5.0115(-1)	8.1270(-1)	1.6443(0)	4.2376(0)	7.4356(0)	1.2494(1)	2.0990(1)	2.9508(1)	4.6573(1)	8.0009(1)	1.1250(2)	1.6025(2)
2500.00	3.6672(-2)	6.6872(-2)	1.2357(-1)	2.4133(-1)	3.8628(-1)	7.6129(-1)	1.8805(0)	3.5818(0)	6.6659(0)	1.2151(1)	1.7686(1)	2.8812(1)	5.1044(1)	7.3053(1)	1.0537(2)
3500.00	1.2481(-2)	2.2616(-2)	4.1380(-2)	7.9446(-2)	1.2513(-1)	2.3962(-1)	5.5945(-1)	1.0095(0)	1.9884(0)	4.3860(0)	7.0879(0)	1.2740(1)	2.4142(1)	3.5753(1)	5.2797(1)
5000.00	3.8704(-3)	6.9734(-3)	1.2644(-2)	2.3902(-2)	3.7103(-2)	6.9306(-2)	1.5533(-1)	2.7040(-1)	5.0223(-1)	1.0647(0)	1.9171(0)	4.2477(0)	9.5089(0)	1.4944(1)	2.3047(1)
6500.00	1.6476(-3)	2.9567(-3)	5.3302(-3)	9.9738(-3)	1.5336(-2)	2.8183(-2)	6.1544(-2)	1.0495(-1)	1.9006(-1)	3.8756(-1)	6.6190(-1)	1.5006(0)	4.1678(0)	7.1827(0)	1.1870(1)
7083.30	1.2471(-3)	2.2352(-3)	4.0221(-3)	7.5028(-3)	1.1503(-2)	2.1033(-2)	4.5563(-2)	7.7211(-2)	1.3880(-1)	2.8025(-1)	4.7429(-1)	1.0459(0)	3.0598(0)	5.4899(0)	9.3508(0)
7083.50	1.2470(-3)	2.2350(-3)	4.0218(-3)	7.5021(-3)	1.1502(-2)	2.1031(-2)	4.5558(-2)	7.7203(-2)	1.3879(-1)	2.8022(-1)	4.7424(-1)	1.0458(0)	3.0594(0)	5.4894(0)	9.3501(0)
8000.00	8.3072(-4)	1.4867(-3)	2.6682(-3)	4.9561(-3)	7.5685(-3)	1.3745(-2)	2.9451(-2)	4.9482(-2)	8.8072(-2)	1.7556(-1)	2.9391(-1)	6.3296(-1)	1.8503(0)	3.6030(0)	6.4864(0)
10000.00	4.3337(-4)	7.5865(-4)	1.3365(-3)	2.4376(-3)	3.6757(-3)	6.5510(-3)	1.3670(-2)	2.2524(-2)	3.9230(-2)	7.6192(-2)	1.2508(-1)	2.6070(-1)	7.0266(-1)	1.4519(0)	3.0202(0)
20000.00	2.0268(-4)	2.9807(-4)	4.4900(-4)	7.1093(-4)	9.8208(-4)	1.5508(-3)	2.7694(-3)	4.0867(-3)	6.2596(-3)	1.0387(-2)	1.5168(-2)	2.6724(-2)	5.7945(-2)	1.0040(-1)	1.8636(-1)
40000.00	6.5940(-4)	9.2456(-4)	1.3230(-3)	1.9880(-3)	2.6536(-3)	3.9867(-3)	6.6580(-3)	9.3349(-3)	1.3362(-2)	2.0102(-2)	2.6881(-2)	4.0554(-2)	6.8358(-2)	9.6784(-2)	1.4060(-1)
80000.00	2.1916(-3)	3.0683(-3)	4.3835(-3)	6.5756(-3)	8.7678(-3)	1.3152(-2)	2.1921(-2)	3.0691(-2)	4.3846(-2)	6.5773(-2)	8.7701(-2)	1.3157(-1)	2.1932(-1)	3.0711(-1)	4.3887(-1)
100000.00	3.1476(-3)	4.4068(-3)	6.2955(-3)	9.4434(-3)	1.2591(-2)	1.8887(-2)	3.1479(-2)	4.4071(-2)	6.2959(-2)	9.4441(-2)	1.2592(-1)	1.8889(-1)	3.1484(-1)	4.4080(-1)	6.2976(-1)
160000.00	5.6760(-3)	7.9465(-3)	1.1352(-2)	1.7028(-2)	2.2704(-2)	3.4057(-2)	5.6761(-2)	7.9465(-2)	1.1352(-1)	1.7028(-1)	2.2704(-1)	3.4057(-1)	5.6762(-1)	7.9467(-1)	1.1352(0)
320000.00	1.2942(-2)	1.8119(-2)	2.5884(-2)	3.8826(-2)	5.1767(-2)	7.7651(-2)	1.2942(-1)	1.8119(-1)	2.5884(-1)	3.8826(-1)	5.1768(-1)	7.7651(-1)	1.2942(0)	1.8119(0)	2.5884(0)
640000.00	2.7207(-2)	3.8089(-2)	5.4413(-2)	8.1620(-2)	1.0883(-1)	1.6324(-1)	2.7207(-1)	3.8089(-1)	5.4413(-1)	8.1620(-1)	1.0883(0)	1.6324(0)	2.7207(0)	3.8089(0)	5.4413(0)
1000000.00	4.0993(-2)	5.7391(-2)	8.1987(-2)	1.2298(-1)	1.6397(-1)	2.4596(-1)	4.0993(-1)	5.7391(-1)	8.1987(-1)	1.2298(0)	1.6397(0)	2.4596(0)	4.0993(0)	5.7391(0)	8.1987(0)

1996ApJ...459..686D

TABLE 5.2

TOTAL ENERGY DEPOSITION IN SILICATE DUST GRAINS

E_γ (eV)	50Å	70Å	100Å	150Å	200Å	300Å	500Å	700Å	1000Å	1500Å	2000Å	3000Å	5000Å	7000Å	1.0 μm
10.00	2.5558(0)	3.7745(0)	5.9243(0)	1.0188(1)	1.3987(1)	1.5793(1)	1.5510(1)	1.4359(1)	1.3014(1)	1.1777(1)	1.1073(1)	1.0284(1)	9.5607(0)	9.2103(0)	8.9228(0)
11.00	3.8363(0)	5.6698(0)	8.8094(0)	1.4098(1)	1.7074(1)	1.7698(1)	1.6625(1)	1.5223(1)	1.3881(1)	1.2615(1)	1.1890(1)	1.1077(1)	1.0331(1)	9.9696(0)	9.6738(0)
12.00	5.9705(0)	8.7896(0)	1.3257(1)	1.8659(1)	1.9688(1)	1.9509(1)	1.7415(1)	1.5966(1)	1.4570(1)	1.3268(1)	1.2522(1)	1.1684(1)	1.0915(1)	1.0543(1)	1.0766(1)
12.73	7.7855(0)	1.1290(1)	1.6294(1)	2.0657(1)	2.0811(1)	2.0366(1)	1.8094(1)	1.6599(1)	1.5167(1)	1.3838(1)	1.3076(1)	1.2222(1)	1.1442(1)	1.1069(1)	1.0781(1)
12.75	7.8327(0)	1.1351(1)	1.6364(1)	2.0699(1)	2.0840(1)	2.0387(1)	1.8113(1)	1.6616(1)	1.5183(1)	1.3854(1)	1.3091(1)	1.2237(1)	1.1457(1)	1.1084(1)	1.0240(1)
13.62	9.5269(0)	1.3566(1)	1.8711(1)	2.1960(1)	2.1916(1)	2.1224(1)	1.8949(1)	1.7390(1)	1.5942(1)	1.4594(1)	1.3823(1)	1.2962(1)	1.2182(1)	1.1811(1)	1.1512(1)
13.64	9.5619(0)	1.3600(1)	1.8739(1)	2.1971(1)	2.1933(1)	2.1241(1)	1.8968(1)	1.7409(1)	1.5962(1)	1.4613(1)	1.3843(1)	1.2982(1)	1.2202(1)	1.1831(1)	1.1532(1)
14.00	1.0025(1)	1.4154(1)	1.9202(1)	2.2153(1)	2.2225(1)	2.1528(1)	1.9304(1)	1.7754(1)	1.6310(1)	1.4964(1)	1.4194(1)	1.3336(1)	1.2560(1)	1.2192(1)	1.2032(1)
14.18	1.0356(1)	1.4588(1)	1.9660(1)	2.2446(1)	2.2499(1)	2.1726(1)	1.9472(1)	1.7909(1)	1.6457(1)	1.5106(1)	1.4334(1)	1.3474(1)	1.2697(1)	1.2328(1)	1.2045(1)
14.20	1.0400(1)	1.4646(1)	1.9725(1)	2.2490(1)	2.2537(1)	2.1751(1)	1.9490(1)	1.7926(1)	1.6472(1)	1.5120(1)	1.4347(1)	1.3487(1)	1.2710(1)	1.2341(1)	1.1895(1)
20.00	1.9870(1)	2.3089(1)	2.4248(1)	2.4287(1)	2.3722(1)	2.2214(1)	1.9997(1)	1.8695(1)	1.7547(1)	1.6529(1)	1.5970(1)	1.5368(1)	1.4848(1)	1.4610(1)	1.4425(1)
30.00	1.0373(1)	1.3074(1)	1.6186(1)	1.9969(1)	2.2313(1)	2.4782(1)	2.6495(1)	2.6928(1)	2.7040(1)	2.6958(1)	2.6846(1)	2.6672(1)	2.6474(1)	2.6367(1)	2.6276(1)
45.00	1.1372(1)	1.4789(1)	1.9174(1)	2.4527(1)	2.8443(1)	3.3495(1)	3.8153(1)	3.9968(1)	4.1037(1)	4.1602(1)	4.1775(1)	4.1856(1)	4.1834(1)	4.1792(1)	4.1792(1)
56.23	1.1621(1)	1.5401(1)	2.0237(1)	2.6650(1)	3.1598(1)	3.8552(1)	4.5766(1)	4.8958(1)	5.1035(1)	5.2267(1)	5.2720(1)	5.6211(1)	5.6230(1)	5.6230(1)	5.6230(1)
56.25	1.1618(1)	1.5401(1)	2.0240(1)	2.6659(1)	3.1610(1)	3.8569(1)	4.5788(1)	4.8982(1)	5.1060(1)	5.2294(1)	5.2747(1)	5.6242(1)	5.6256(1)	5.6257(1)	5.6257(1)
68.03	1.3609(1)	1.8111(1)	2.3834(1)	3.1650(1)	3.7740(1)	4.6346(1)	5.5396(1)	5.9445(1)	6.2105(1)	6.3702(1)	6.7872(1)	6.8041(1)	6.8061(1)	6.8062(1)	6.8062(1)
68.05	1.3602(1)	1.8103(1)	2.3825(1)	3.1641(1)	3.7730(1)	4.6336(1)	5.5386(1)	5.9436(1)	6.2096(1)	6.3693(1)	6.7865(1)	6.8033(1)	6.8053(1)	6.8054(1)	6.8054(1)
90.00	1.3554(1)	1.8247(1)	2.4629(1)	3.3748(1)	4.1330(1)	5.2920(1)	6.6943(1)	7.4288(1)	7.9723(1)	8.7883(1)	8.9150(1)	8.9853(1)	9.0011(1)	9.0017(1)	9.0018(1)
101.00	1.3234(1)	1.7966(1)	2.4487(1)	3.4003(1)	4.2098(1)	5.4900(1)	7.1320(1)	8.0550(1)	8.7808(1)	9.7513(1)	9.9471(1)	1.0067(2)	1.0100(2)	1.0102(2)	1.0102(2)
101.02	1.3235(1)	1.7968(1)	2.4489(1)	3.4005(1)	4.2101(1)	5.4905(1)	7.1329(1)	8.0562(1)	8.7824(1)	9.7530(1)	9.9491(1)	1.0069(2)	1.0102(2)	1.0104(2)	1.0104(2)
108.66	1.6138(1)	2.1884(1)	2.9687(1)	4.0860(1)	5.0177(1)	6.4463(1)	8.1782(1)	9.0898(1)	9.7624(1)	1.0364(2)	1.0632(2)	1.0807(2)	1.0863(2)	1.0868(2)	1.0868(2)
108.68	1.6016(1)	2.1799(1)	2.9623(1)	4.0815(1)	5.0145(1)	6.4440(1)	8.1768(1)	9.0892(1)	9.7612(1)	1.0505(2)	1.0708(2)	1.0830(2)	1.0863(2)	1.0865(2)	1.0865(2)
120.00	1.5540(1)	2.1359(1)	2.9281(1)	4.0794(1)	5.0573(1)	6.5993(1)	8.5634(1)	9.6623(1)	1.1002(2)	1.1607(2)	1.1825(2)	1.1956(2)	1.1990(2)	1.1992(2)	1.1992(2)
140.00	1.4858(1)	2.0619(1)	2.8604(1)	4.0473(1)	5.0841(1)	6.7898(1)	9.1277(1)	1.0562(2)	1.2271(2)	1.3238(2)	1.3628(2)	1.3892(2)	1.3981(2)	1.3990(2)	1.3991(2)
200.00	1.1960(1)	1.7093(1)	2.4330(1)	3.5585(1)	4.5983(1)	6.4502(1)	9.4188(1)	1.1715(2)	1.4162(2)	1.6608(2)	1.7930(2)	1.9134(2)	1.9797(2)	1.9939(2)	1.9982(2)
250.00	9.2136(0)	1.3489(1)	1.9638(1)	2.9308(1)	3.8475(1)	5.5466(1)	8.4193(1)	1.0892(2)	1.3847(2)	1.7342(2)	1.9627(2)	2.2189(2)	2.4071(2)	2.4637(2)	2.4894(2)
291.00	7.4417(0)	1.1187(1)	1.6583(1)	2.5126(1)	3.3298(1)	4.8724(1)	7.5101(1)	9.9394(1)	1.3015(2)	1.6978(2)	1.9867(2)	2.3550(2)	2.6842(2)	2.8061(2)	2.8724(2)
291.02	7.4409(0)	1.1186(1)	1.6582(1)	2.5124(1)	3.3295(1)	4.8721(1)	7.5097(1)	9.9390(1)	1.3014(2)	1.6978(2)	1.9867(2)	2.3551(2)	2.6843(2)	2.8062(2)	2.8726(2)
350.00	5.5179(0)	8.6867(0)	1.3242(1)	2.0545(1)	2.7532(1)	4.0921(1)	6.3339(1)	8.5664(1)	1.1555(2)	1.5715(2)	1.9068(2)	2.3952(2)	2.9354(2)	3.1905(2)	3.3604(2)
500.00	2.5066(0)	4.4929(0)	7.6380(0)	1.2692(1)	1.7626(1)	2.4722(1)	4.1966(1)	5.8424(1)	8.1901(1)	1.1812(2)	1.5066(2)	2.0692(2)	2.9116(2)	3.4863(2)	4.0386(2)
537.27	2.2834(0)	4.1951(0)	7.3488(0)	1.2507(1)	1.7501(1)	2.2317(1)	3.8201(1)	5.3481(1)	7.5359(1)	1.0963(2)	1.4091(2)	1.9599(2)	2.8225(2)	3.4423(2)	4.0746(2)
537.29	4.7113(0)	8.6515(0)	1.5628(1)	2.7894(1)	3.9647(1)	5.6354(1)	9.7965(1)	1.3567(2)	1.8523(2)	2.5416(2)	3.0750(2)	3.8303(2)	4.6401(2)	4.9882(2)	5.2088(2)
650.00	4.1301(0)	7.2091(0)	1.2826(1)	2.2958(1)	2.8397(1)	4.6150(1)	8.1037(1)	1.1378(2)	1.5864(2)	2.2485(2)	2.8082(2)	3.6909(2)	4.8330(2)	5.4643(2)	5.9571(2)
720.68	3.4010(0)	5.8669(0)	1.0365(1)	1.8651(1)	2.4799(1)	4.0414(1)	7.1465(1)	1.0092(2)	1.4216(2)	2.0444(2)	2.5900(2)	3.4945(2)	4.7667(2)	5.5583(2)	6.2482(2)
720.70	4.5346(0)	7.8365(0)	1.3948(1)	2.5504(1)	3.3800(1)	5.5732(1)	9.8792(1)	1.3944(2)	1.9469(2)	2.7425(2)	3.4059(2)	4.4184(2)	5.6562(2)	6.3037(2)	6.7713(2)
850.00	5.4337(0)	9.2039(0)	1.5975(1)	2.5183(1)	3.7190(1)	6.1481(1)	1.0917(2)	1.5478(2)	2.1713(2)	3.0738(2)	3.8365(2)	5.0197(2)	6.5011(2)	7.3067(2)	7.9082(2)
1100.00	3.2424(0)	5.8554(0)	1.0577(1)	1.7253(1)	2.5812(1)	4.3390(1)	7.8532(1)	1.1306(2)	1.6220(2)	2.3809(2)	3.0715(2)	4.2670(2)	6.1032(2)	7.3870(2)	8.6529(2)
1294.40	1.9483(0)	3.6566(0)	6.4451(0)	1.2477(1)	1.9119(1)	3.2994(1)	6.1175(1)	8.9113(1)	1.2956(2)	1.9345(2)	2.5359(2)	3.6241(2)	5.4416(2)	6.8679(2)	8.4591(2)
1294.60	2.3163(0)	4.2432(0)	7.3452(0)	1.4159(1)	2.1829(1)	3.8318(1)	7.2819(1)	1.0725(2)	1.5704(2)	2.3572(2)	3.0896(2)	4.3748(2)	6.4295(2)	7.9366(2)	9.5039(2)
1350.00	2.2147(0)	4.0222(0)	6.7432(0)	1.3119(1)	2.0326(1)	3.5879(1)	6.8503(1)	1.0116(2)	1.4857(2)	2.2388(2)	2.9450(2)	4.1998(2)	6.2459(2)	7.7922(2)	9.4518(2)
1500.00	1.7660(0)	3.1465(0)	5.2880(0)	1.0574(1)	1.6644(1)	2.9929(1)	5.8066(1)	8.6407(1)	1.2790(2)	1.9472(2)	2.5810(2)	3.7405(2)	5.7158(2)	7.3050(2)	9.1403(2)
1828.40	9.7916(-1)	1.6610(0)	3.1225(0)	6.4120(0)	1.0539(1)	2.0009(1)	4.0755(1)	6.2035(1)	9.3637(1)	1.4533(2)	1.9557(2)	2.8992(2)	4.6176(2)	6.1146(2)	8.0261(2)
1828.60	1.3444(0)	2.1875(0)	3.9533(0)	7.8401(0)	1.2686(1)	2.4004(1)	4.9759(1)	7.7018(1)	1.1791(2)	1.8491(2)	2.4969(2)	3.7134(2)	5.8405(2)	7.6231(2)	9.7785(2)
2000.00	1.2231(0)	1.9029(0)	3.4018(0)	6.6254(0)	1.0692(1)	2.0507(1)	4.3340(1)	6.7642(1)	1.0439(2)	1.6492(2)	2.2396(2)	3.3629(2)	5.3711(2)	7.1134(2)	9.2973(2)
2500.00	6.1172(-1)	1.0696(0)	1.9625(0)	3.8833(0)	6.2837(0)	1.2322(1)	2.7728(1)	4.4839(1)	7.1088(1)	1.1498(2)	1.5863(2)	2.4343(2)	4.0209(2)	5.4818(2)	7.4639(2)
3500.00	2.1507(-1)	3.6627(-1)	6.5827(-1)	1.3077(0)	2.1516(0)	4.4258(0)	1.0875(1)	1.9212(1)	3.3278(1)	5.7935(1)	8.2848(1)	1.3255(2)	2.2947(2)	3.2317(2)	4.5752(2)
5000.00	7.3955(-2)	1.2412(-1)	2.1940(-1)	4.2655(-1)	6.8840(-1)	1.3632(0)	3.2706(0)	5.9028(0)	1.1132(1)	2.2415(1)	3.5090(1)	6.1472(1)	1.1455(2)	1.6734(2)	2.4499(2)
6500.00	3.3724(-2)	5.6158(-2)	9.8414(-2)	1.8930(-1)	3.0290(-1)	5.9105(-1)	1.3806(0)	2.4153(0)	4.3820(0)	8.9487(0)	1.5144(1)	3.0150(1)	6.2647(1)	9.5531(1)	1.4470(2)
7083.30	2.6049(-2)	4.3280(-2)	7.5656(-2)	1.4509(-1)	2.3158(-1)	4.5006(-1)	1.0442(0)	1.8153(0)	3.2594(0)	6.5114(0)	1.1007(1)	2.2919(1)	5.0037(1)	7.7971(1)	1.1991(2)
7083.50	1.1776(-1)	1.9789(-1)	3.4986(-1)	6.6704(-1)	1.0371(0)	1.8730(0)	3.8424(0)	6.1709(0)	1.0176(1)	1.8393(1)	2.8902(1)	5.5874(1)	1.2130(2)	1.9191(2)	2.9917(2)
8000.00	1.1134(-1)	1.9557(-1)	3.6537(-1)	7.4300(-1)	1.1765(0)	2.1301(0)	4.2512(0)	6.6271(0)	1.0516(1)	1.8003(1)	2.6930(1)	4.9467(1)	1.0534(2)	1.6602(2)	2.5863(2)
10000.00	5.4459(-2)	9.3376(-2)	1.6873(-1)	3.3125(-1)	5.2920(-1)	1.0078(0)	2.2880(0)	4.0628(0)	7.2684(0)	1.3350(1)	2.0225(1)	3.6067(1)	7.5414(1)	1.1961(2)	1.8784(2)
20000.00	7.4361(-3)	1.2489(-2)	2.2083(-2)	4.2173(-2)	6.5737(-2)	1.1941(-1)	2.4805(-1)	4.0320(-1)	6.7589(-1)	1.2434(0)	1.9649(0)	3.8752(0)	9.4128(0)	1.7167(1)	3.3239(1)
40000.00	1.9068(-3)	2.9266(-3)	4.7043(-3)	8.1606(-3)	1.2015(-2)	2.0409(-2)	3.9296(-2)	6.0753(-2)	9.6476(-2)	1.6620(-1)	2.5011(-1)	4.5986(-1)	1.0149(0)	1.6977(0)	2.9071(0)
80000.00	3.2639(-3)	4.6001(-3)	6.6339(-3)	1.0082(-2)	1.3575(-2)	2.0636(-2)	3.4980(-2)	4.9593(-2)	7.1862(-2)	1.1000(-1)	1.4960(-1)	2.3307(-1)	4.1319(-1)	6.0424(-1)	9.0422(-1)
100000.00	4.5243(-3)	6.3494(-3)	9.1017(-3)	1.3718(-2)	1.8357(-2)	2.7671(-2)	4.6408(-2)	6.5276(-2)	9.3746(-2)	1.4169(-1)	1.9034(-1)	2.8972(-1)	4.9479(-1)	7.0494(-1)	1.0261(0)
160000.00	8.6707(-3)	1.2143(-2)	1.7354(-2)	2.6046(-2)	3.4743(-2)	5.2146(-2)	8.6977(-2)	1.2184(-1)	1.7416(-1)	2.6148(-1)	3.4896(-1)	5.2437(-1)	8.7658(-1)	1.2298(0)	1.7609(0)
320000.00	2.0037(-2)	2.8053(-2)	4.0076(-2)	6.0116(-2)	8.0157(-2)	1.2024(-1)	2.0041(-1)	2.8058(-1)	4.0084(-1)	6.0129(-1)	8.0176(-1)	1.2027(0)	2.0049(0)	2.8072(0)	4.0107(0)
640000.00	4.1065(-2)	5.7491(-2)	8.2130(-2)	1.2320(-1)	1.6426(-1)	2.4639(-1)	4.1065(-1)	5.7492(-1)	8.2131(-1)	1.2320(0)	1.6426(0)	2.4640(0)	4.1067(0)	5.7494(0)	8.2135(0)
1000000.00	6.0946(-2)	8.5325(-2)	1.2189(-1)	1.8284(-1)	2.4379(-1)	3.6568(-1)	6.0947(-1)	8.5325(-1)	1.2189(0)	1.8284(0)	2.4379(0)	3.6568(0)	6.0947(0)	8.5326(0)	1.2189(1)

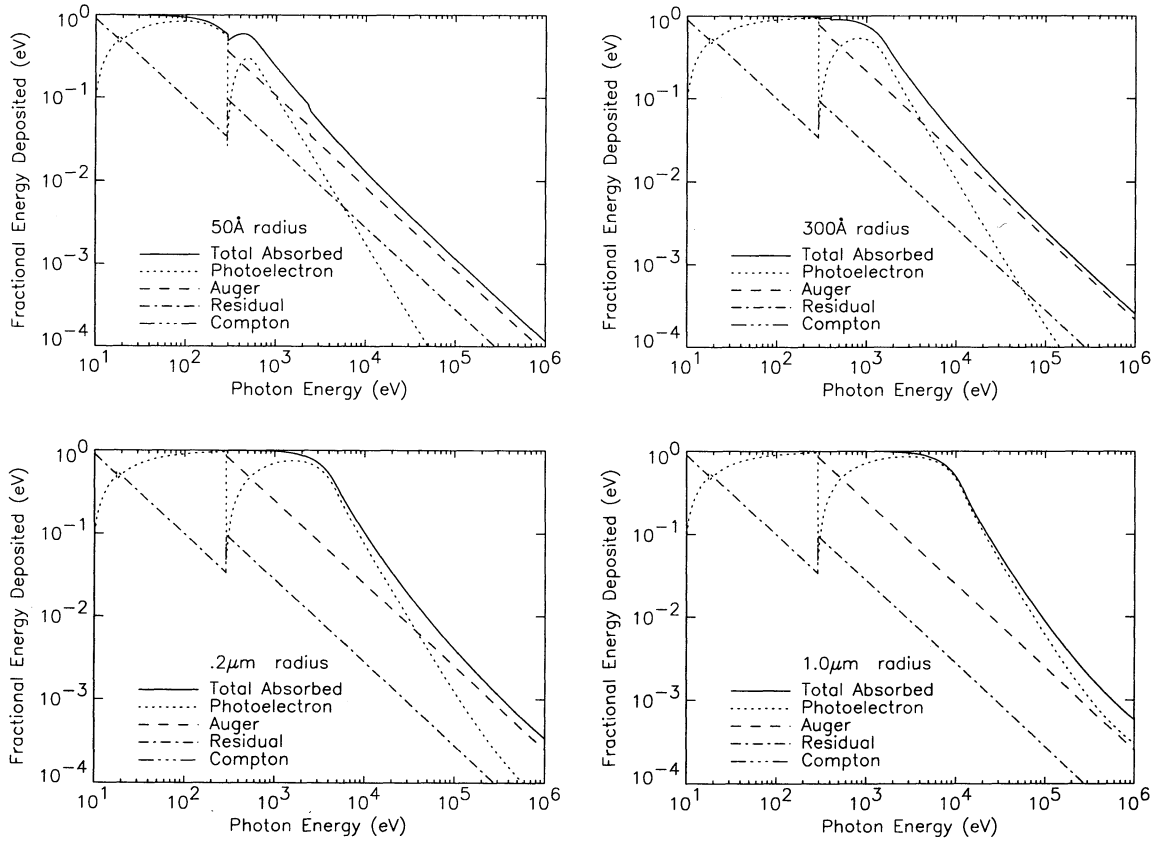

FIG. 4.—Fraction of the energy of the absorbed photon that is deposited in the dust, $E_{dep}(a, E_\gamma)/E_\gamma$, is plotted vs. incident photon energy for graphite grains of radii $a = 0.005, 0.03, 0.2$, and $1.0\ \mu$m.

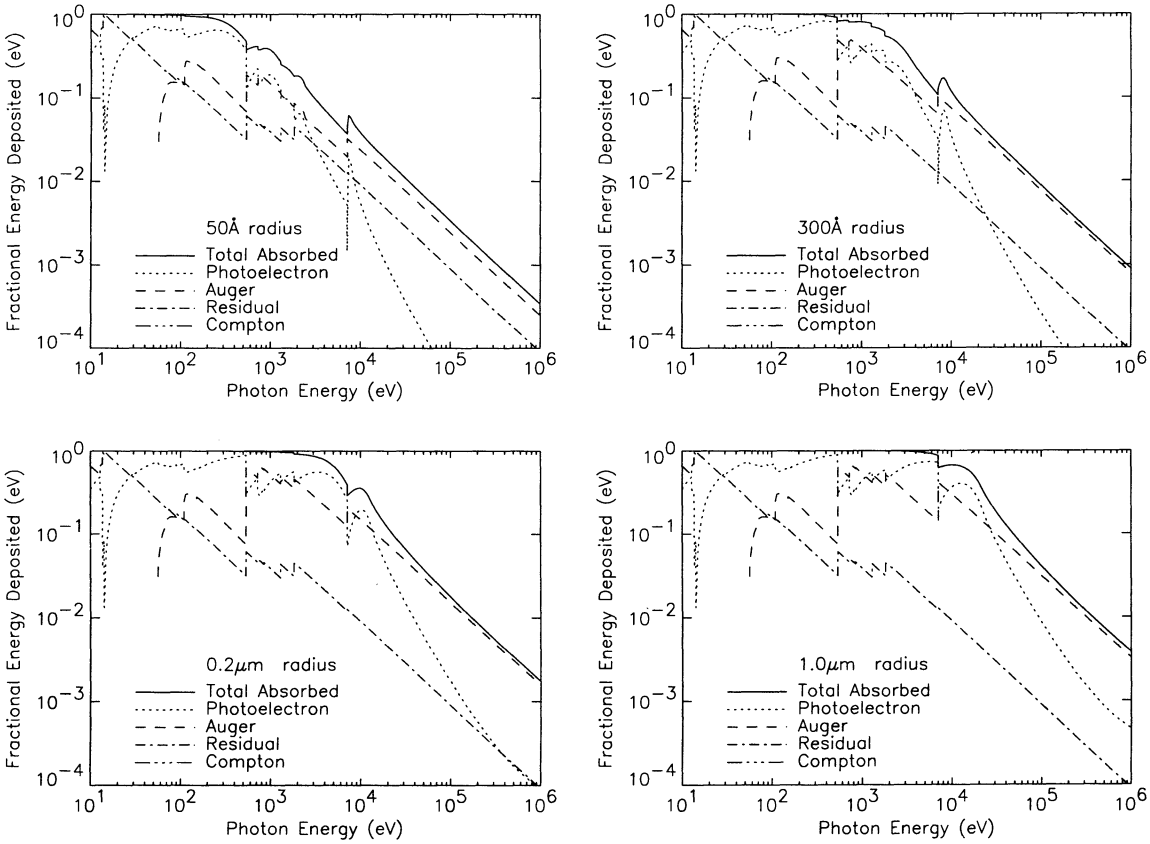

FIG. 5.—Same as Fig. 4 for silicate grains

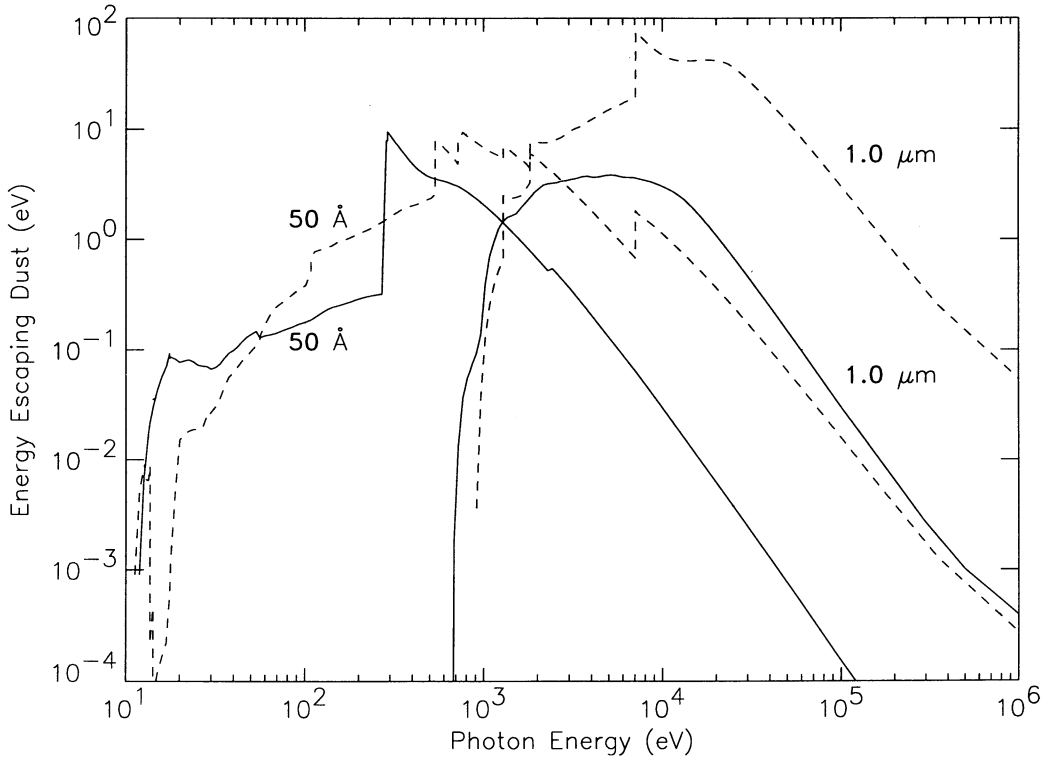

FIG. 6.—Energy carried away by escaping electrons is shown as a function of incident photon energy for 50 Å radius graphite grains (*solid line*) and silicate grains (*dashed line*).

Stoutamire for his advice in programing the Auger cascade calculations. We also thank Peter Martin for sending us the UV optical constants used in our Mie calculations; the referee, Mike Shull, for his helpful comments; and Ari Laor for a useful discussion. An electronic version of Table 5 is available upon request from Randy Smith at rsmith@wisp5.physics.wisc.edu. This research was supported by NASA's Infrared Astrophysics Research Program, RTOP No. 188-44-53-05. R. K. S. acknowledges support by the NSF Graduate Student Fellowship.

REFERENCES

Agarwal, B. K. 1979, X-Ray Spectroscopy (New York: Springer)
Arendt, R. G. 1991, AJ, 101, 2160
Berger, J. M., & Seltzer, S. M. 1964, Tables of Energy Losses and Ranges of Electrons and Positrons (NASA SP-3012) (Washington: NASA)
Compton, A. H., & Allison, S. K. 1935, X-Rays in Theory and Experiment (New York: van Nostrand)
Cullen, D. E., Chen, M. H., Hubbell, J. H., Perkins, S. T., Plechaty, E. F., Rathkopf, J. A., & Scofield, J. H. 1989, Tables and Graphs of Photon-Interaction Cross Sections from 10 eV to 100 GeV Derived from the LLNL Evaluated Photon Data Library (EPDL), UCRL-50400, Vol. 6, Part A, Rev. 4
Draine, B. T., & Woods, D. T. 1991, ApJ, 383, 621
Dwek, E. 1985, ApJ, 297, 719
———. 1987, ApJ, 322, 812
Dwek, E., & Arendt, R. G. 1992, ARA&A, 30, 11
Dwek, E., & Werner, M. W. 1981, ApJ, 248, 138
Henke, B. L., Lee, P., Tanaka, T. J., Shimabukuro, R. L., & Fujikawa, B. K. 1982, Atomic Data Nucl. Data Tables, 27, 1
Iskef, H., Cunningham, J. W. & Watt, D. E. 1983, Phys. Medical Biology, 28, 535
Jacobs, V. L., Davis, J., Rozsnyai, B. F., & Cooper, J. W. 1980, Phys. Rev. A, 21, 1917
Jacobs, V. L., & Rozsnyai, B. F. 1986, Phys. Rev. A, 34, 216
Laor, A., & Draine, B. T. 1993, ApJ, 402, 441
Lee, P., Rathkopf, J., Cullen, D., & Perkins, S. 1990, Tables of Average Distributions of Particles Emitted by Ionized Elements (Z = 6–100), UCID-21918
Opendak, M. G. 1990, A&A, 165, 9
Reif, F. 1965, Fundamentals of Statistical and Thermal Physics (New York: McGraw-Hill)
Rouleau, F., & Martin, P. G. 1991, ApJ, 377, 526
Shull, J. M. 1979, ApJ, 234, 761
———. 1980, ApJ, 237, 769
Smith, R. K., & Dwek, E. 1996, in preparation
Verner, D. A., & Yakovlev, D. G. 1995, A&AS, 109, 125
Voit, G. M. 1991, ApJ, 379, 122
Watson, W. D. 1973, J. Opt. Soc. Am., 63, 164
Wheeler, J. C., Mazurek, T. J., & Sivaramakrishnan, A. 1980, ApJ, 237, 781